

Beyond Inverted Pendulums: Task-optimal Simple Models of Legged Locomotion

Yu-Ming Chen¹, Jianshu Hu² and Michael Posa¹

Abstract—Reduced-order models (ROM) are popular in online motion planning due to their simplicity. A good ROM captures the bulk of the full model’s dynamics while remaining low dimension. However, planning within the reduced-order space unavoidably constrains the full model, and hence we sacrifice the full potential of the robot. In the community of legged locomotion, this has lead to a search for better model extensions, but many of these extensions require human intuition, and there has not existed a principled way of evaluating the model performance and discovering new models. In this work, we propose a model optimization algorithm that automatically synthesizes reduced-order models, optimal with respect to any user-specified cost function. To demonstrate our work, we optimized models for a bipedal robot Cassie. We show in hardware experiment that the optimal ROM is simple enough for real time planning application and that the real robot achieves higher performance by using the optimal ROM.

Index Terms—Reduced-order models, model optimization, humanoid and bipedal locomotion, optimization and optimal control, real time planning and control

I. INTRODUCTION

State-of-the-art approaches to model-based planning and control of legged locomotion can be categorized into two types [1]. One uses the full-order model of a robot, and the other uses a reduced-order model (ROM). With the full model, we can leverage our full knowledge about the robot to achieve high performance [2]–[4]. However, this comes with the cost of heavy computation load, and it also poses a challenge in formal analysis, because modern legged robots have many degrees of freedom. To manage this complexity, the community of legged robots has embraced the use of reduced-order models.

Most reduced-order models adopt constraints (assumptions) on the full model dynamics and approximate the full-order dynamics with reduced-order dynamics³. For example, the linear inverted pendulum (LIP) model [7], [8] assumes that the robot is a point mass that stays in a plane, which greatly reduces energy efficiency and limits the speed and stride length of the robot. The spring loaded inverted pendulum (SLIP) model [9] is a point mass model with spring-mass dynamics, which implies zero centroidal angular momentum rate and

¹The authors are with the General Robotics, Automation, Sensing and Perception (GRASP) Laboratory, University of Pennsylvania, Philadelphia, PA 19104, USA. {yminchen, posa}@seas.upenn.edu

²The author is with the UM-SJTU Joint Institute, Shanghai Jiao Tong University, Shanghai, China. hjs1998@sjtu.edu.cn

³One exception is the centroidal momentum model [5], [6]. It describes the actual dynamics of the robot and does not impose any constraint on the full dynamics. However, in order to plan for the centroidal momentum model, we still need to involve the full model configuration or state in the planning problem.

zero impacts at foot touchdown. Therefore, when we plan for motions in the reduced-space only, we unavoidably impose limitations on the full dynamics. This restricts a complex robot’s motion to that of the low-dimensional model and necessarily sacrifices performance of the robot.

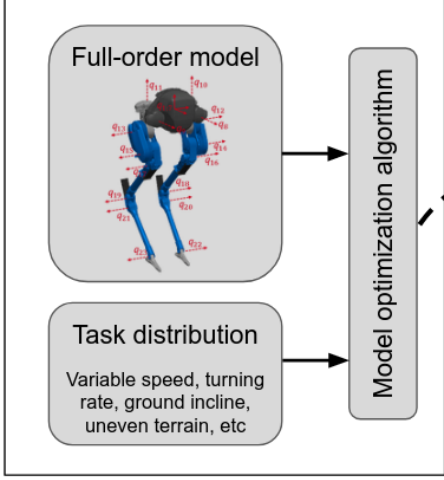
The above limitations of the reduced-order models have long been acknowledged by the community, resulting in a wide array of extensions that universally rely on human intuition, and are often in the form of mechanical components (a spring, a damper, a rigid body, the second leg, etc) [10]–[17]. The success of such model extensions which enable high-performance real time planning on hardware are listed as follows. Chignoli et al. [18] used the single rigid body model and assumed small body pitch and roll angle, in order to formulate a convex planning problem. Xiong et al. [10] extended LIP with a double-support phase and assumed zero foot touchdown impact, so the model is still linear and conducive to a LQR controller [19]–[21]. Gibson et al. [22], [23] used the angular-momentum-based LIP which has better prediction accuracy than the traditional LIP. Dai et al. and Herzog et al. [24], [25] combined the centroidal momentum model with full robot configurations, and its real time application in planning was made possible thanks to Boston Dynamics’ software engineering [26].

Although some of the above extensions have successfully improved the robot performance, it is still not clear which extension provides more performance improvement than the others, and we do not have a metric to improve the model performance with. Additionally, it has been shown that not all model extensions can significantly improve the performance of robots. For example, allowing the center of mass height to vary provides limited aid in the task of balancing [27], [28]. In our work, we aim to automatically discover the most beneficial extension of the reduced-order models by directly optimizing the ROM given a user-specified objective function and a task distribution.

A. Related Work

Some researchers improve the performance of the reduced-order model by mixing it with a full model in the planning horizon of a model predictive control (MPC). Li et al. [29] broke the planning horizon into two segments. They used a full model for the immediate horizon and a reduced-order model for the far horizon. Norby et al. [30] mixed the full and reduced-order models while adaptively switching between the models. Our work is different from these existing works in that we directly optimize a reduced-order model instead of

Offline model generation (Section III)



Real time planning and control (Section IV)

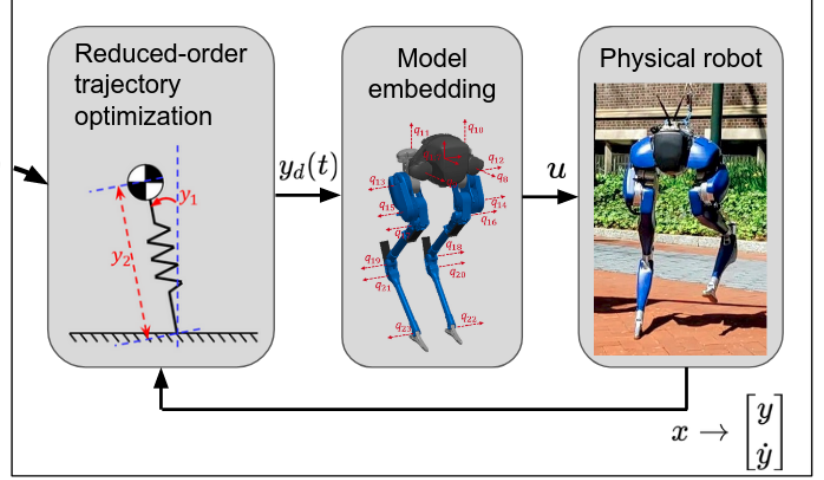


Fig. 1. An outline of the synthesis and deployment of optimal reduced-order models (ROM). Offline, given a full-order model and a distribution of tasks, we optimize a new model that is effective over the task space (Section III). Online, we generate new plans for the reduced-order model and track these trajectories on the true, full-order system (Section IV). This diagram also shows the bipedal robot Cassie (in the rightmost box) and its full model. Cassie has five motors on each leg – three located at the hip, one at the knee and one at the toe. Additionally, there are 2 leaf springs in each leg, and the spring joints are visualized by q_{16} to q_{19} in the figure. The springs are a part of the closed-loop linkages of the legs. We model these linkages with distance constraints, so there are no rods visualized in the model.

reasoning about scheduling two models to improve the overall model performance.

Pandala et al. [31] attempted to close the gap between the full model and the reduced-order model, where they modeled the difference between the two models as a disturbance to the reduced dynamics. Our prior work [32] optimized for the Angular Center of Mass model by minimizing the angular momentum error between the reduced-order model and full model. Different from these two pieces of work, in this paper we optimize a model with respect to a generic user-specified objective function instead of some particular metric like the gap between two models. Additionally, we optimize both the reduced-order dynamics and the embedding function (a projection operation from the full model to the reduced-order model). This is different from Pandala et al. [31] which only optimized for the dynamics, and also different from our prior work [32] which only optimized for the embedding function. Lastly, we embed the reduced-order model exactly along the full model trajectories during optimization, while Pandala et al. [31] approximated the embedding where the embedding error depended on the feedback controller.

B. Contributions

The contributions of this paper are:

- 1) We propose a bilevel optimization algorithm to automatically synthesize new reduced order models, embedding high-performance capabilities within low-dimensional representations. (This contribution was presented in the conference form [33] of this paper.)
- 2) We improve the model formulation of the prior work [33], and improve the algorithm efficiency by using the Envelope Theorem to derive the analytical gradient of

an optimization problem. We provide more examples of model optimization, with different sizes of task space and basis functions.

- 3) We design a real time model predictive controller (MPC) for the optimal ROM, and demonstrate that the optimal model is capable of achieving higher performance in both simulation and hardware experiment of a bipedal robot Cassie.
- 4) We evaluate and compare the performances of reduced-order models in both simulation and hardware experiments. We analyze the performance gain and discuss the lessons learned in translating the model performance of an open-loop system to a closed-loop system.

C. Organization

The paper is organized as follows. Section II introduces the models of the Cassie robot and the background for this paper. Section III introduces our definition of a reduced-order model, formulates the model optimization problem, provides an algorithm that solves the problem, and finally demonstrates model optimization with a few examples. Section IV introduces an MPC for a specific class of ROM's used in Section V. Section V compares and analyzes the performance improvement in trajectory optimization, in simulation and in hardware. Section VI discusses the hybrid nature of legged robot dynamics and introduces the MPC for a general ROM. Finally, we discuss some of the lessons learned during the journey of realizing better performance on the robot in Section VII, and conclude the paper in Section VIII.

II. BACKGROUND

A. Reduced-order Models of Legged Locomotion

Modern legged robots like the Agility Robotics Cassie have many degrees of freedom and may have passive dynamic elements such as springs and dampers. To manage this complexity and simplify the design of planning and control, the community has embraced the use of reduced-order models. A good reduced-order model is a low-dimensional representation that captures much of the relevant dynamics while enabling effective control design, a concept closely related to that of templates and anchors [34], [35].

One observation, common to many approaches, lies in the relationship between foot placement, ground reaction forces, and the center of mass (CoM). While focusing on the CoM neglects the individual robot limbs, controlling the CoM position has proven to be an excellent proxy for the stability of a walking robot. CoM-based simple models include the LIP [7], [8], SLIP [9], hopping models [36], inverted pendulums [37], [38], and others. Since these models are universally low-dimensional, they have enabled a variety of control synthesis and analysis techniques that would not otherwise be computationally tractable. For example, numerical methods have been successful at finding robust gaits and control designs [39]–[42], and assessing stability [43].

A popular approach of using reduced-order models on legged robots is to first plan with the ROM to get desired ROM trajectories and desired foot steps, and then use a low-level controller to track the planned trajectories. The work flow is shown in the right half of Fig. 1. When the planning speed becomes fast enough (e.g. by reducing the model complexity), we can solve the planning problem with a receding horizon in real time, which is called the Model Predictive Control (MPC).

B. Models of Cassie

The bipedal robot Cassie (Fig. 1) is the platform we used to test our model optimization algorithm. Here we briefly introduce its full model. Let the state of Cassie be $x = [q, v] \in \mathbb{R}^{45}$ where $q \in \mathbb{R}^{23}$ and $v \in \mathbb{R}^{22}$ are generalized position and velocity, respectively. We note that q and v have different dimensions, because the floating base orientation is expressed via quaternion. The conversion between q and v depends only on q [44].

The standard equations of motion are

$$M\dot{v} = f_{cg}(q, v) + Bu + J^T\lambda + \tau_{app}(q, v) \quad (1)$$

where M is the mass matrix which includes the reflected inertia of motors, f_{cg} contains the velocity product terms and the gravitational term, B is the actuation selection matrix, u is the actuator input, J is the Jacobian of holonomic constraints associated with the constraint forces λ , and τ_{app} includes all the other generalized forces applied on the system such as joint damping forces and leaf spring forces in the knees and ankles. In the case of walking, we assume the swing foot collision is perfectly inelastic, so the robot dynamics model is hybrid.

Combining the discrete impact dynamics (from foot collision) with Eq. (1), we derive the hybrid equations of motion

$$\begin{cases} \dot{x} = f(x, u), & x^- \notin S \\ x^+ = \Delta(x^-, \Lambda), & x^- \in S \end{cases} \quad (2)$$

where x^- and x^+ are pre- and post-impact state, Λ is the impulse of swing foot collision, Δ is the discrete mapping of the touchdown event, and S is the surface in the state space where the event must occur [45], [46].

Cassie's legs contain four four-bar linkages, two around the shin links and the other two around the tarsus links. We simplify the model by lumping the mass of the rods of the tarsus four-bar linkages into the toe bodies, while the shin linkages are modeled with fixed-distance constraints. To simplify the model further for the trajectory optimization in Section II-C, we assume Cassie's springs are infinitely stiff (or equivalently no springs), in which case $q \in \mathbb{R}^{19}$ and $v \in \mathbb{R}^{18}$. This assumption has been successfully deployed by other researchers [47], and it is necessary for the coarse integration steps in our trajectory optimization. We will call the model without springs as the *simplified Cassie model*, and the model with springs as the *Cassie model*.

C. Trajectory Optimization

This paper will heavily leverage trajectory optimization within the inner loop of a bilevel optimization problem. We briefly review it here, but the reader is encouraged to see [48] for a more complete description. Generally speaking, trajectory optimization is a process of finding state $x(t)$ and input $u(t)$ that minimize some measure of cost h while satisfying a set of constraints C . Following the approach taken in prior work [49], [50], we explicitly optimize over state, input, and constraint (contact) forces $\lambda(t)$,

$$\begin{array}{ll} \min_{x(t), u(t), \lambda(t)} & \int_{t_0}^{t_f} h(x(t), u(t)) dt \\ \text{s.t.} & \dot{x}(t) = f(x(t), u(t), \lambda(t)), \\ & C(x(t), u(t), \lambda(t)) \leq 0, \end{array} \quad (3)$$

where f is the dynamics of the system, λ are the forces required to satisfy holonomic constraints, and t_0 and t_f are the initial and the final time respectively. Standard approaches discretize in time, formulating (3) as a finite-dimensional nonlinear programming problem. For the purposes of this paper, any such method would be appropriate, while we use DIRCON [50] to address the closed kinematic chains of the Cassie robot. DIRCON transcribes the infinite dimensional problem in Eq. (3) into a finite dimensional nonlinear problem

$$\begin{array}{ll} \min_w & \sum_{i=1}^{n-1} \frac{1}{2} (h(x_i, u_i) + h(x_{i+1}, u_{i+1})) \delta_k \\ \text{s.t.} & f_c(x_i, x_{i+1}, u_i, u_{i+1}, \lambda_i, \lambda_{i+1}, \delta_i, \alpha_i) = 0, \\ & i = 1, \dots, n-1 \\ & C(x_i, u_i, \lambda_i) \leq 0, \quad i = 1, \dots, n \end{array} \quad (4)$$

where n is the number of knot points, f_c is the collocation constraint for dynamics, and the decision variables are

$$\begin{aligned} w = & [x_1, \dots, x_n, u_1, \dots, u_n, \lambda_1, \dots, \lambda_n, \\ & \delta_1, \dots, \delta_{n-1}, \alpha_1, \dots, \alpha_{n-1}] \in \mathbb{R}^{n_w}. \end{aligned}$$

where δ_i 's are time intervals, and α_i 's are slack variables specific to DIRCON.

A large-scale nonlinear optimization problem such as (4) can be difficult to solve. To improve the convergence of the solve, we manually scale the decision variables, constraints and the cost function, and we also add regularization terms (see Appendix A for details).

D. Bilevel Optimization

Since our formulation can be broadly categorized as bilevel optimization [51], we here briefly review its basics. The basic structure of our bilevel optimization problem is written as

$$\min_{\theta} \left[\sum_i \min_w \Psi_i(\theta, w) \right] \quad (5)$$

The goal is to minimize the outer-level objective function $\sum_i \Psi_i(\theta, w_i^*(\theta))$ with respect to θ , where $w_i^*(\theta)$ is obtained by minimizing the inner-level objective $\Psi_i(\theta, w)$ parameterized by θ . Bilevel optimization has recently been used in various applications such as meta-learning [52], reinforcement learning [53], robotics [54], [55], etc.

Solving a bilevel program is generally NP-hard [56]. There are two types of methods to approach bilevel optimization. The first type is constraint-based [57], [58], where the key idea is to replace the inner level optimization with its optimality condition (such as the KKT conditions [59]), and finally solve a “single-level” constrained optimization. However, those methods are difficult to apply to the problem of this paper, because our inner-level is a trajectory optimization, and replacing it with its optimality condition will additionally introduce a large number of dual variables and co-states, dramatically increasing the size of the ‘single-level’ optimization. The second type is gradient-based [60], [61]. The idea is to maintain and solve the inner-level optimization, and then update the outer-level decision variable by differentiating through the inner-level solution using ‘graph-unrolling’ approximation [61], [62] or implicit theorem [63]. Compared to constraint-based methods, gradient-based methods maintain the bilevel structure and make bilevel optimization more tractable and efficient to solve.

In this paper, we use the Envelope theorem [64], [65] and exploit the fact that our problem uses the same objective functions in the outer level and the inner level. This structure enables us to develop a more efficient gradient-based method (the second type) to solve our problem. Specifically, the gradient of the outer-level objective does not require differentiating the solution of the inner-level optimization with respect to the parameters. This leads to two numerical advantages of our method over existing gradient-based methods. First, our method bypasses the computationally intensive implicit theorem, which requires the inverse of hessian of the inner-level optimization. Second, our method leverages the inner-loop solver’s understanding of active and inactive constraints, avoiding implementing the algorithm ourselves and avoiding tuning parameters such as the active set tolerance.

III. MODEL OPTIMIZATION

In this section, we propose a definition of reduced-order models, along with a notion of quality (or cost) for such

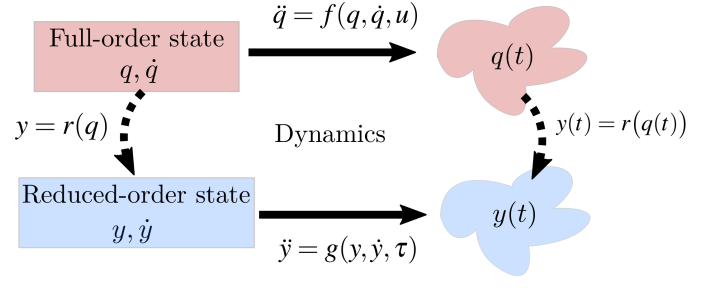


Fig. 2. Relationship of the full-order and reduced-order models. The generalized positions q and y satisfy the embedding function r for all time, and the evolution of the velocities \dot{q} and \dot{y} respects the dynamics f and g , respectively.

models. We then introduce a bilevel optimization algorithm to optimize within our class of models.

A. Definition of Reduced-order Models

Let q and u be the generalized position and input of the full-order model, and let y and τ be the generalized position and input of the reduced-order model. We define a reduced-order model μ of dimension n_y by two functions – an embedding function $r : q \mapsto y$ and the second-order dynamics of the reduced-order model $g(y, \dot{y}, \tau)$. That is,

$$\mu \triangleq (r, g), \quad (6)$$

with

$$y = r(q), \quad (7a)$$

$$\ddot{y} = g(y, \dot{y}, \tau), \quad (7b)$$

where $\dim y < \dim q$ and $\dim \tau \leq \dim u$. As an example, to represent SLIP, r is the spring length and the spring angle with respect to the normal direction of ground, g is the spring-mass dynamics, and $\dim \tau = 0$ as SLIP is passive.

The embedding function r can explicitly include the left or right leg of the robot (e.g. choosing left leg as support leg instead of right leg), in which case there will be two reduced-order models. In this paper, we assume to parameterize over left-right symmetric reduced order models. As such, we explicitly optimize over a model corresponding to left-support, which will then be mirrored to cover both left and right-support phases. The details of this mirroring operation are in Appendix B.

There is an alternative definition of a reduced-order model which restricts the model’s state to a manifold, as opposed to our definition in Eq. 6 which restricts the dynamics (flow) of the state. Our definition is a broader definition of ROM, and one of its advantages is that the ROM dynamics enables the ability to plan only within the reduced-order state space. Fig. 2 shows the relationship between the full-order and the reduced-order models. If we integrate the two models forward in time with their own dynamics, the resultant trajectories will still satisfy the embedding function r at any time in the future.

B. Problem Statement

As shown in the left half of Fig. 1, the goal is to find an optimal model μ^* , given a distribution Γ over a set of tasks. The distribution could be provided *a priori* or estimated via the output of a higher-level motion planner. The tasks might include anything physically achievable by the robot, such as walking up a ramp at different speeds, turning at various rates, jumping, running with a specified amount of energy, etc. The goal, then, is to find a reduced-order model that enables low-cost motion over the space of tasks,

$$\mu^* = \operatorname{argmin}_{\mu \in M} \mathbb{E}_\gamma [\mathcal{J}_\gamma(\mu)], \quad (8)$$

where M is the model space, \mathbb{E}_γ takes the expected value over Γ , and $\mathcal{J}_\gamma(\mu)$ is the cost required to achieve the tasks $\gamma \sim \Gamma$ while the robot is restricted to a particular model μ .

With our model definition in Eq. (6), the problem in Eq. (8) is infinite dimensional over the space of embedding and dynamics functions, r and g . To simplify, we parametrize r and g with basis functions $\{\phi_{e,i} \mid i = 1, \dots, n_e\}$ and $\{\phi_{d,i} \mid i = 1, \dots, n_d\}$ with linear weights $\theta_e \in \mathbb{R}^{n_y \cdot n_e}$ and $\theta_d \in \mathbb{R}^{n_y \cdot n_d}$. Further assuming that the dynamics are affine in τ with constant multiplier, r and g are given as

$$y = r(q; \theta_e) = \Theta_e \phi_e(q), \quad (9a)$$

$$\ddot{y} = g(y, \dot{y}, \tau; \theta_d) = \Theta_d \phi_d(y, \dot{y}) + B_y \tau, \quad (9b)$$

where $\Theta_e \in \mathbb{R}^{n_y \times n_e}$ and $\Theta_d \in \mathbb{R}^{n_y \times n_d}$ are θ_e and θ_d arranged as matrices, $\phi_e = [\phi_{e,1}, \dots, \phi_{e,n_e}]$, $\phi_d = [\phi_{d,1}, \dots, \phi_{d,n_d}]$, and $B_y \in \mathbb{R}^{n_y \times n_\tau}$. While we choose linear parameterization here, any differentiable function approximator (e.g. a neural network) can be equivalently used.

Let the model parameters be $\theta = [\theta_e, \theta_d] \in \mathbb{R}^{n_t}$. We can rewrite Eq. (8) as

$$\theta^* = \operatorname{argmin}_\theta \mathbb{E}_\gamma [\mathcal{J}_\gamma(\theta)]. \quad (O)$$

From now on, we work explicitly in θ , rather than μ .

C. Task Evaluation

We use trajectory optimization to evaluate the task cost $\mathcal{J}_\gamma(\theta)$. Under this setting, the tasks γ are defined by a cost function h_γ and task-specific constraints C_γ . $\mathcal{J}_\gamma(\theta)$ is the optimal cost to achieve the tasks while simultaneously respecting the embedding and dynamics given by θ . We note that the cost function h_γ is a function of the full model, although we occasionally refer to the cost evaluated by this function as the ROM performance because the ROM is embedded in the full model.

The resulting optimization problem is similar to (4), but contains additional constraints and decision variables for the reduced-order model embedding,

$$\begin{aligned} \mathcal{J}_\gamma(\theta) \triangleq \min_w & \sum_{i=1}^{n-1} \frac{1}{2} (h_\gamma(x_i, u_i) + h_\gamma(x_{i+1}, u_{i+1})) \delta_k \\ \text{s.t.} & f_c(x_i, x_{i+1}, u_i, u_{i+1}, \lambda_i, \lambda_{i+1}, \delta_i) = 0, \\ & g_c(x_i, u_i, \lambda_i, \tau_i; \theta) = 0, \quad i = 1, \dots, n-1 \\ & C_\gamma(x_i, u_i, \lambda_i) \leq 0, \quad i = 1, \dots, n \end{aligned} \quad (\text{TO})$$

Algorithm 1 Reduced-order model optimization

Input: Task distribution Γ and step size α

Output: θ^*

Model initialization

1: $\theta \leftarrow \theta_0$

Model optimization

2: **repeat**

3: Sample N tasks from $\Gamma \Rightarrow \gamma_j, j = 1, \dots, N$

4: **for** $j = 1, \dots, N$ **do**

5: Solve (TO) to get $\mathcal{J}_{\gamma_j}(\theta)$

6: Compute $\nabla_\theta [\mathcal{J}_{\gamma_j}(\theta)]$ by Eq. (10)

7: **end for**

8: Average the gradients $\Delta\theta = \frac{\sum_{j=1}^N \nabla_\theta [\mathcal{J}_{\gamma_j}(\theta)]}{N}$

9: *Gradient descent* $\theta \leftarrow \theta - \alpha \cdot \Delta\theta$

10: **until** convergence

11: **return** θ

where f_c and g_c are dynamics constraints for the full-order and reduced-order dynamics, respectively. The decision variables are $w = [x_1, \dots, x_n, u_1, \dots, u_n, \lambda_1, \dots, \lambda_n, \tau_1, \dots, \tau_n, \delta_1, \dots, \delta_{n-1}, \alpha_1, \dots, \alpha_{n-1}]$, noting the addition of τ_i .

The formulation of dynamics and holonomic constraints of the full-order model are described in [50], while the reduced-order constraint g_c is

$$\begin{aligned} g_c &= \ddot{y}_i - g(y_i, \dot{y}_i, \tau_i; \theta_d) = 0 \\ \Rightarrow g_c &= J_i \dot{v}_i + \dot{J}_i v_i - g(y_i, \dot{y}_i, \tau_i; \theta_d) = 0 \end{aligned}$$

where

$$y_i = r(q_i; \theta_e),$$

$$\dot{y}_i = \frac{\partial r(q_i; \theta_e)}{\partial q_i} \dot{q}_i,$$

$$\dot{v}_i = M^{-1} (f_{cg}(q_i, v_i) + B u_i + J^T \lambda_i + \tau_{app}(q_i, v_i)).$$

The constraint $g_c = 0$ not only explicitly describes the dynamics of the reduced-order model but also implicitly imposes the embedding constraint r via the dummy variables y and \dot{y} . Therefore, the problem (TO) is equivalent to simultaneous optimization of full-order and reduced-order trajectories that must also be consistent with the embedding r .

D. Bilevel Optimization Algorithm

Since there might be a large or infinite number of tasks $\gamma \sim \Gamma$ in Eq. (O), solving for the exact solution is often intractable. Therefore, we use stochastic gradient descent to solve Eq. (O) (specifically in the outer optimization, as opposed to the inner trajectory optimization). That is, we sample a set of tasks from the distribution Γ and optimize the averaged sample cost over the model parameters θ .

The full approach to (O) is outlined in Algorithm 1. Starting from an initial parameter seed θ_0 , N tasks are sampled, and the cost for each task $\mathcal{J}_{\gamma_j}(\theta)$ is evaluated by solving the corresponding trajectory optimization problem (TO).

To compute the gradient $\nabla_\theta [\mathcal{J}_{\gamma_j}(\theta)]$, we previously [33] adopted an approach based in sequential quadratic programming. It introduced extra parameters (e.g. tolerance for determining active constraints) and required solving a potentially

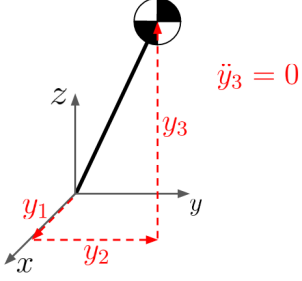


Fig. 3. The linear inverted pendulum (LIP) model. It is a point mass model of which height is restricted in a plane. The point mass and the origin of this model correspond to the center of mass and the stance foot of the robot, respectively. In the examples of this paper, we initialize the reduced-order model to the LIP model during model optimization.

large and ill-conditioned system of linear equations which can take minutes to solve to good accuracy. Here, we take a new approach where we derive the analytical gradient $\nabla_{\theta} [\mathcal{J}_{\gamma_j}(\theta)]$ shown in Lemma 1 (also see Section II-D).

The model optimization in Algorithm 1 is deemed to have converged if the norm of the average gradient of the sampled costs falls below a specified threshold.

Lemma 1. *Let $\tilde{f}_{\gamma}(w, \theta) \leq 0$ encapsulate all the constraints of (TO). Under some conditions⁴, the gradient of the optimal cost of (TO) with respect to θ is given by*

$$\nabla_{\theta} [\mathcal{J}_{\gamma}(\theta)] = \lambda^{*T} \frac{\partial \tilde{f}_{\gamma}(w^*, \theta)}{\partial \theta}, \quad (10)$$

where w^* and λ^* are respectively the primal and the dual solution to the optimization problem (TO).

Proof. The proof follows directly from the Envelope Theorem [65], noting the cost in (TO) is independent of θ . \square

E. Examples of Model Optimization

In the trajectory optimization problem in Eq. (TO), we assume the robot walks with instantaneous change of support. That is, the robot transitions from right support to left support instantaneously, and vice versa. We consider only half-gait periodic motion, and so include right-left leg alternation in the impact map Δ .

We solve the problems (TO) in parallel in each iteration of Algorithm 1 using the SNOPT toolbox [66]. All examples were generated using the Drake software toolbox [67] and source code is freely available⁵.

1) Initialization and parameterization of ROM: To demonstrate Algorithm 1, we optimize for 3D reduced-order models on Cassie. The models are initialized with a three-dimensional LIP, of which the generalized position y is shown in Fig. 3. For reference, the equations of motion of the 3D LIP model are

$$\ddot{y} = \begin{bmatrix} \ddot{y}_1 \\ \ddot{y}_2 \\ \ddot{y}_3 \end{bmatrix} = \begin{bmatrix} c_g \cdot y_1/y_3 \\ c_g \cdot y_2/y_3 \\ 0 \end{bmatrix}, \quad (11)$$

⁴The condition is that the optimal solution to problem (TO) satisfies the KKT conditions [59]. This condition is mild in practice.

where c_g is the gravitational acceleration constant. This model represents a point-mass body, where the body has a constant speed in the vertical direction.

We choose basis functions such that they not only explicitly include the position of the LIP, but also include a diverse set of additional terms. That is, the basis set ϕ_e includes the CoM position relative to the stance foot, and monomials of $\{1, q_7, \dots, q_{19}\}$ up to n_{ϕ} -th order. Similarly, the feature set ϕ_d includes the terms in LIP dynamics (i.e. $c_g y_1/y_3$ and $c_g y_2/y_3$) and monomials of $\{1, y_1, y_2, y_3, \dot{y}_1, \dot{y}_2, \dot{y}_3\}$ up to n_{ϕ} -th order. With these basis functions, the ROM parameters θ can be trivially initialized to match the LIP model's.

2) Optimization Examples and Result: We demonstrate a few examples of model optimization and compare their results. Examples are

- 1 : The baseline example ($u^T u$ cost function, 2D task space, $n_{\phi} = 2$),
- 2 : Monomial order $n_{\phi} = 4$,
- 3 : $\dot{v}^T \dot{v}$ cost function,
- 4 : Same as Example 3 except that we only use the harder tasks to train ROM,
- 5 : Large 4D task space,

and the detailed settings are shown in Table I.

The cost function h_{γ} was chosen to be the weighted sum of squares of the robot input u , the generalized velocity v and acceleration \dot{v} . In Examples 1, 2 and 5, we heavily penalize the input term which is a proxy of a robot's energy consumption. On the other hand, we heavily penalize the acceleration \dot{v} in Examples 3 and 4. We observed that Cassie's motions with the initial ROM's are very similar among all examples. In contrast, the motions with optimal ROM's are mostly dependent on the cost function h_{γ} , given the same ROM parameterization. Compared to Example 1, the optimal motion of Example 3 shows more vertical pelvis movement. The motions of these examples are shown in the accompanying video⁵ for both the initial ROM and optimal ROM.

The optimization results are shown in Fig. 4, where the costs are normalized by the optimal cost of (TO) without ROM embedding (i.e. without the constraints g_c). Therefore, the costs are lower-bounded by 1. In Fig. 4, Examples 1 and 2 share the same starting cost, because they have the same training task range. We can also see that parameterizing the ROM with 2nd order monomial seems sufficient for the task space of Examples 1 and 2, since the normalized cost is close to 1. However, using higher order of monomials helps the cost to converge faster in the beginning.

Since the initial cost of Example 3 is much higher than Example 1's, we can say that the LIP model is a more restrictive model under the performance metric of Example 3 than that of 1. Additionally, Example 4's task space is a subset of Example 3's, specifically the part of the task space with bigger stride length. We would expect the LIP model does not perform well with big stride length, and indeed Fig. 4 shows that the initial cost of Example 4 is higher than that of Example 3. Fortunately, a high initial cost provides us with a bigger room of potential improvement. As we see in Table

⁵ <https://sites.google.com/view/ymchen/research/optimal-rom>

Example #	1	2	3	4	5
Stride length (m)		[-0.4, 0.4]		[0.3, 0.4]	[-0.4, 0.4]
Pelvis height (m)			[0.87, 1.03]		[0.84, 1.06]
Ground incline (rad)			0		[-0.15, 0.15]
Turning rate (rad/s)			0		[-0.3, 0.3]
Stride duration (s)			0.35		0.35
Monomial order n_ϕ	2	4	2	2	2
Dominant cost in J_γ	u	u	\dot{v}	\dot{v}	u
Cost reduction	22.8%	20.7%	27.6%	38.2%	16.5%

TABLE I

A FEW EXAMPLES OF MODEL OPTIMIZATION. THE TABLE INCLUDES THE RANGE OF TASKS USED TO TRAIN THE MODELS, THE HIGHEST ORDER OF THE MONOMIALS OF BASIS FUNCTIONS, THE DOMINANT TERM IN THE COST FUNCTION J_γ , AND THE COST REDUCTION (THE COST IMPROVEMENT RELATIVE TO THE COST OF THE INITIAL MODEL).

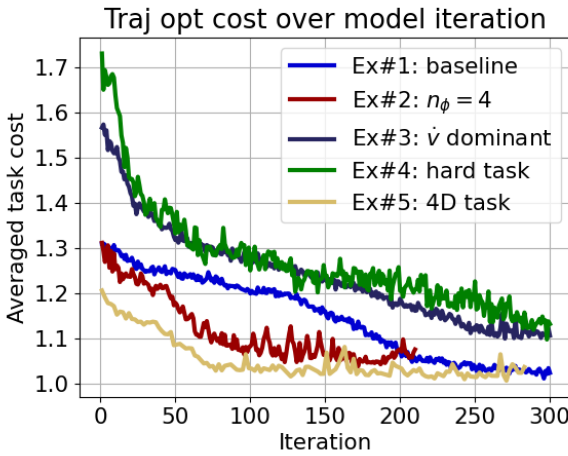


Fig. 4. The averaged cost of the sampled tasks of each model optimization iteration in Examples 1 to 5. Costs are normalized by the cost associated with the full-order model (i.e. the cost of full model trajectory optimization without any reduced-order model embedding). Therefore, the costs cannot go below 1. The costs at iteration 1 represent the averaged costs for the robots with the embedded initial reduced-order models, LIP. Note that the empirical average does not strictly decrease, as tasks are randomly sampled and are of varying difficulty.

I, Example 3 has higher cost reduction than Example 1, and Example 4 has the highest cost reduction.

In Example 5, both the task space dimension and the task range are increased, and the algorithm was again able to find an optimal model. The optimized models are capable of expressing more input-efficient motions than the LIP model, better leveraging the natural dynamics of Cassie⁵. The reduced-order model optimization improves the performance of the robot, while maintaining the model simplicity. We note that the optimal model, unlike its classical counterpart, does not map easily to a physical model, if the embedding function r contains abstract basis functions such as monomials. While this limits our ability to attach physical meaning to y and τ , it is a sacrifice that one can make to improve performance beyond that of hand-designed approaches.

IV. MPC FOR A SPECIAL CLASS OF ROM

After a reduced order model is optimized, we use it on the robot to achieve desired tasks, as depicted in Fig. 1. Specifically, we design a real time model predictive controller (MPC) with the reduced-order model derived in Section III.

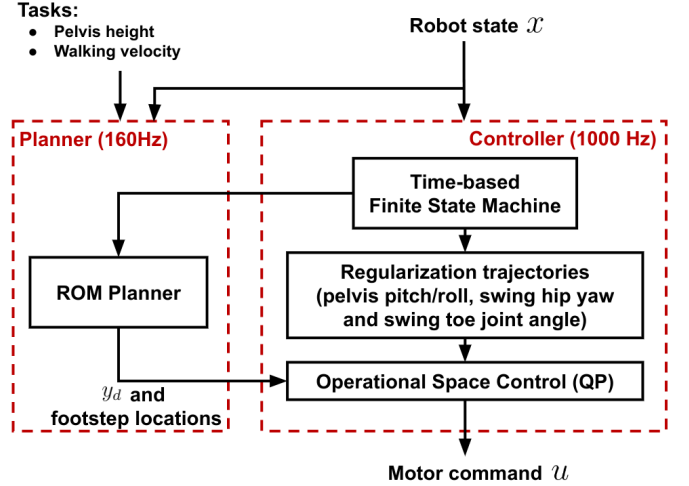


Fig. 5. The diagram of the model predictive control (MPC) introduced in Section IV. The MPC is composed of two processes – the controller process and the planner process. The high-level planner solves for the desired reduced-order model (ROM) trajectories and swing foot stepping locations. The regularization trajectories are used inside the controller process to fill out the joint redundancy of the robot. For reduced-order models without body orientation (e.g. CoM model without moment of inertia), we send the pelvis yaw velocity command directly to the controller process. All desired trajectories are sent to the Operational Space Controller (OSC) which is a quadratic-programming based inverse-dynamics controller [68], [69].

The controller structure is shown in Fig. 5. It contains a high-level planner in the reduced-order space (Section IV-A) and a low-level tracking controller in the full-order space (Section IV-B). The high-level planner receives the robot state and tasks, and plans for the desired ROM trajectory and the footsteps of the robot. The controller tracks these desired trajectory and footsteps, while internally using nominal trajectories to handle the system redundancy.

In this and the following sections (Section IV and V), we assume the embedding function r is fixed to be the center of mass position relative to the stance foot, meaning that we only optimize for the ROM dynamics g and not the embedding function r during model optimization. This simplifies the planning problem and enables a richer performance analysis in Section V, since the models are physically interpretable. The planner for a general ROM will be introduced in Section VI.

A. Planning with Reduced-order Models

We formulate a reduced-order trajectory optimization problem to walk n_s strides, using direct collocation method described in Section II-C to discretize the trajectory into n knot points. Under the premise that the ROM embedding r is the CoM, we further assume the ROM does not have continuous inputs τ (e.g. center of pressure) but it has discrete inputs $\tau_{fp} \in \mathbb{R}^2$ which is the stepping location of the swing foot relative to the stance foot. Let $z = [y, \dot{y}] \in \mathbb{R}^{2n_y}$, and let z^- and z^+ be the reduced state of pre- and post-touchdown event, respectively. The discrete dynamics is

$$z^+ = z^- + B_{fp} \tau_{fp} \quad (12)$$

with

$$B_{fp} = \begin{bmatrix} -1 & 0 & 0 & 0 & 0 & 0 \\ 0 & -1 & 0 & 0 & 0 & 0 \end{bmatrix}^\top.$$

The first two rows of Eq. (12) correspond to the change in stance foot reference for the COM position. The last three rows are derived from the assumption of zero ground impact at the foot touchdown event.

To improve readability, we stack decision variables into bigger vectors $z = [y, \dot{y}] \in \mathbb{R}^{2n_y}$, $Z = [z_0, z_1, \dots, z_n] \in \mathbb{R}^{2n_y(n+1)}$, and $T_{fp} = [\tau_{fp,1}, \dots, \tau_{fp,n_s}] \in \mathbb{R}^{2n_s}$. The cost function of the planner is quadratic and expressed in terms of Z and T_{fp} . The planning problem is

$$\begin{aligned} \min_{Z, T_{fp}} \quad & \|Z - Z_d\|_{W_Z}^2 + \|T_{fp}\|_{W_T}^2 \\ \text{s.t.} \quad & \text{ROM continuous dynamics (Eq. (7b)),} \\ & \text{ROM discrete dynamics (Eq. (12)),} \\ & C_{kinematics}(Z, T_{fp}) \leq 0, \\ & z_0 = \text{current feedback reduced-order state,} \end{aligned} \quad (13)$$

where $W_{(.)}$'s are the weights of the norms, Z_d is a stack of desired states which encourage the robot to reach a goal location and regularize velocities, and $C_{kinematics} \leq 0$ is the constraints on step lengths and stepping locations relative to the CoM. After solving Eq. (13), we reconstruct the desired ROM trajectory $y_d(t)$ from the optimal solution Z^* , and we construct desired swing foot trajectories from T_{fp}^* with cubic splines.

B. Operational Space Controller

A controller commonly used in legged robots is the quadratic-programming-based operational space controller (QP-based OSC), which is also referred to as the QP-based whole body controller [68], [69]. Assume there are N_y number of outputs $y_i^{osc}(q)$, with desired outputs $y_{i,d}^{osc}(t)$, where $i = 1, 2, \dots, N_y$. For each output (neglecting the subscript i), we can derive the commanded acceleration as the sum of the feedforward acceleration of the desired output and a PD control law

$$\ddot{y}_{cmd}^{osc} = \ddot{y}_d^{osc} + K_p(y_d^{osc} - y^{osc}) + K_d(\dot{y}_d^{osc} - \dot{y}^{osc}).$$

At a high level, the OSC solves for robot inputs that minimize the output tracking errors, while respecting the full model dynamics and constraints (essentially an “MPC” but with

zero time horizon). The optimal control problem of OSC is formulated as

$$\min_{\dot{v}, u, \lambda, \epsilon} \quad \sum_{i=1}^{n_y} \|\ddot{y}_i^{osc} - \ddot{y}_{i,cmd}^{osc}\|_{W_i}^2 + \|u\|_{W_u}^2 + \|\epsilon\|_{W_\epsilon}^2 \quad (14a)$$

$$\text{s.t. } \ddot{y}_i^{osc} = J_i \dot{v} + \dot{J}_i v, \quad i = 1, \dots, N_y \quad (14b)$$

$$\text{Dynamics constraint (Eq. (1))} \quad (14c)$$

$$0 = J_h \dot{v} + \dot{J}_h v \quad (14d)$$

$$\epsilon = J_c \dot{v} + \dot{J}_c v \quad (14e)$$

$$u_{min} \leq u \leq u_{max} \quad (14f)$$

$$\text{Contact force constraints} \quad (14g)$$

where $\|\cdot\|_W$ is the weighted 2-norm, (14d) contains the distance constraint for Cassie's four-bar linkages and the fixed springs constraint, (14e) is the relaxed contact constraints, and (14g) includes friction cone constraints, non-negative normal force constraints and force blending constraints for stance leg transition.

Table II shows all trajectories tracked by the OSC and their corresponding gains and cost weights. The trajectories of the reduced-order model, pelvis orientation and swing foot position are all 3 dimensional, while the hip yaw joint and toe joint of the swing foot are 1 dimensional. The symbols (x,y,z) in Table II indicate the components of the tracking target. They do not necessarily mean the physical (x, y, z) axes for the reduced-order model, since the model optimization might produce a physically non-interpretable model embedding r .

In the existing literature of bipedal robots, robot's floating base position (sometimes the CoM position) and orientation are often chosen to be control targets. They have 6 degrees of freedom (DoF) in total. In the case of fully-actuated robots (i.e. robots with flat feet), there is enough control authority to servo both the position and orientation. For underactuated robots, the existing approaches often give up tracking the trajectories in the transverse plane (x and y axis), because it is not possible to instantaneously track trajectories whose dimension is higher than the number of actuators (or we have to trade off the tracking performance). In this case, motion planning for discrete footstep locations is used to regulate the underactuated DoF. In our control problem, we also face the same challenge since Cassie has line feet. The total dimension of the desired trajectories in Table II is 11, while Cassie only has 10 actuators. Following the common approach, we choose not to track the second element of the ROM in OSC, because it corresponds to the lateral position of the CoM for the initial model (a competing tracking objective to the pelvis roll angle) and maintaining a good pelvis roll tracking is crucial for stable walking. Instead, the second element of ROM is regulated by the desired swing foot locations via the planner in Eq. (13), even though the OSC does not explicitly track it.

C. Hardware Setup and Solve Time

We implement the MPC in Fig. 5 using the Drake toolbox [67], and the code is publicly available on Github⁵. In hardware experiment, the MPC planner runs on a laptop equipped with Intel i7 11800H, and everything else (low-level controller,

Trajectory y_i^{osc}	dim y_i^{osc}	cost weight W			K_p			K_d		
		x	y	z	x	y	z	x	y	z
reduced order model	3	0.1	0	10	10	0	50	0.2	0	1
pelvis orientation	3	2	4	0.02	200	200	0	10	10	10
swing foot position	3	4	4	4	150	150	200	1	1	1
swing leg hip yaw joint	1	0.5			100			2		
swing leg toe joint	1	2			1500			10		

TABLE II
TRAJECTORIES AND GAINS IN THE OPERATIONAL SPACE CONTROL (OSC)

	(R1) no ROM	(R2) initial ROM	(R3) optimal ROM
(C1) Traj. Opt. with simplified Cassie	X	X	X
(C2) Simulation with simplified Cassie		X	X
(C3) Simulation with Cassie		X	X
(C4) Experiment on real Cassie		X	X

TABLE III
EXPERIMENTS CONDUCTED IN SECTION V (MARKED WITH X)

state estimator, etc) on Cassie’s onboard computer. These two computers communicate via LCM [70]. A human sends walking velocity commands to Cassie with a remote controller. Cassie is able to stably walk around with both the initial ROM and the optimal ROM (shown in the accompanying video⁵).

The planning horizon was set to 2 foot steps with stride duration being 0.4 seconds. With cubic spline interpolation between knot points, we found that 4 knot points per stride was sufficient. IPOPT [71] was used to solve the planning problem in Eq. (13), and the solve time was on average around 6 milliseconds with warm-starts. We observed that this solve time was independent of the reduced-order models (initial or optimal) in our experiments. In contrast to the ROM, similar code required tens of seconds for the simplified Cassie model for a single foot step. As the following sections will show, Cassie’s performance (with respect to the user-defined cost function) with the optimal model is better than with the initial model. This demonstrates that the use of ROM greatly reduces planning speed, and that the optimized ROM improves the performance of the robot.

V. PERFORMANCE EVALUATION AND COMPARISON

In this section, we evaluate the performance of the robot (with respect to a user-specified cost function h_γ in Section III-C) in the following ROM settings:

- (R1) without reduced-order model embedding,
- (R2) with initial reduced-order model embedding,
- (R3) with optimal reduced-order model embedding.

Additionally, the evaluation is done in the following cases:

- (C1) trajectory optimization with simplified Cassie (open-loop),
- (C2) simulation with simplified Cassie (closed-loop),
- (C3) simulation with Cassie (closed-loop),

(C4) hardware experiment with real Cassie (closed-loop), where the trajectory optimization in (C1) is the same as the one in Eq. (TO). Environment (C1) is labeled as open-loop and others as closed-loop, because trajectory optimization is an optimal control method where the control inputs and feasible state trajectories are simultaneously solved for, and there is no feedback controller required. Table III lists the experiments conducted in this section. We note that (R1) is only evaluated in (C1), because (R1) is used as an idealized benchmark for comparison.

A. Experiment Motivations

As mentioned in Section II-B, there are physical springs in Cassie’s legs, so we have both the simplified Cassie model (without springs) and Cassie model (with springs). In the model optimization stage, we use the simplified Cassie model, because Cassie’s springs are stiff which demands higher knot point density in trajectory optimization in Eq. (TO), making the problem harder to solve⁶. In contrast, we use both models in the simulation evaluation.

1) *Motivation for (C1):* In Section III, we optimized for a reduced-order model given a task distribution, but we have not seen the performance for out-of-distribution tasks. Additionally, this environment provides the ideal performance benchmark for the closed-loop system to compare to.

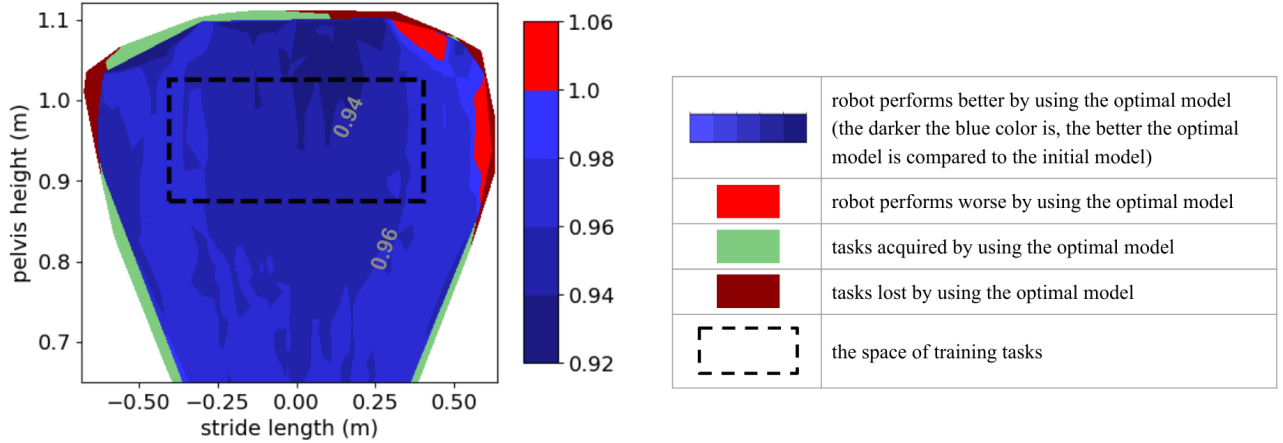
2) *Motivation for (C2):* Trajectory optimization is used in Eq. (TO) to find the optimal model based on the open-loop performance. We want to see how well the cost reduction in open-loop can be translated to the closed-loop system with the MPC from Section IV.

3) *Motivation for (C3) and (C4):* Since the model was optimized using the simplified Cassie model, we also want to know how well the performance can be translated to a model of higher fidelity. Similarly, we are interested to see the performance improvement on the hardware Cassie.

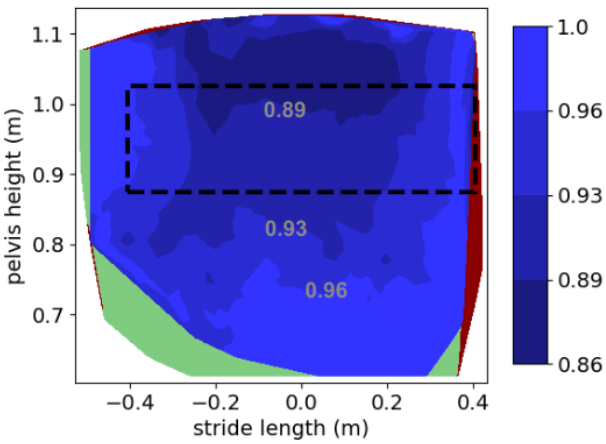
B. Experiment Setups

As mentioned in Section IV, we limit these experiments to ROM’s whose embedding function r is fixed to be the center of mass position relative to the stance foot (see Section VII for general ROM’s). This simplifies the planner and enables a richer performance analysis since the models are physically interpretable.

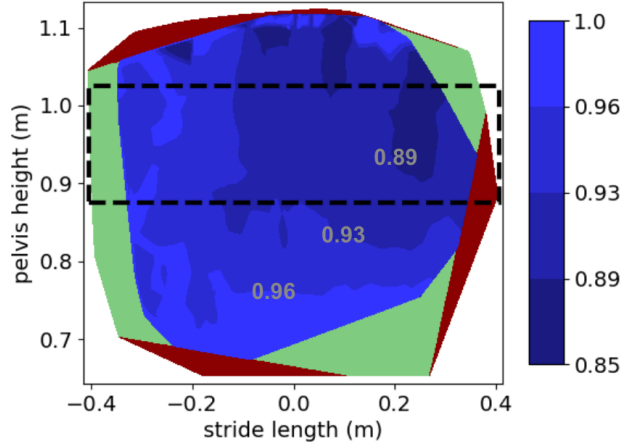
⁶Reher et al. [72] showed 7 times increase in solve time when using the full Cassie model in trajectory optimization. Additionally, Cassie’s spring properties can change over time and are hard to identify accurately, which discourages researchers with Cassie from using the spring model.



(a) Trajectory optimization with the simplified Cassie model, (C1).



(b) Simplified Cassie simulation, (C2).



(c) Cassie simulation, (C3).

Fig. 6. Cost comparison between the initial model (R2) and the optimal model (R3). Each plot shows the ratio of the optimal model's cost to the initial model's cost. The color codes are listed in the table at the top right of this figure.

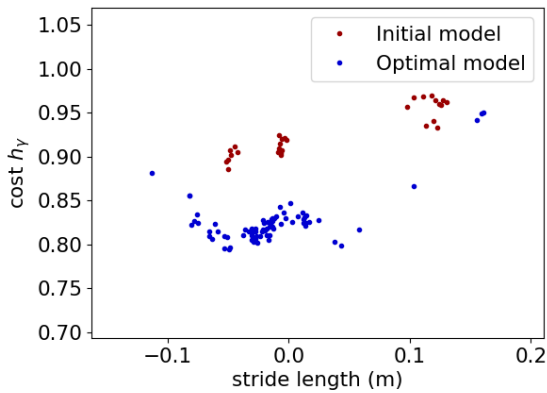


Fig. 7. Cost comparison between the initial model (R2) and the optimal model (R3) on hardware (C4). In the experiment, we used a remote control to walk Cassie around. Then we applied a moving window of 4 foot steps to extract periodic gaits for cost evaluation. We note that there was about 2 cm of height variation in the experiment, but we normalized every extracted data point to the same height (0.9m) using the height-cost relationship from the trajectory optimization to make fair comparisons. The experiment videos can be found in the accompanying video of this paper⁵.

In all experiments of this section, we use models from the same model optimization (i.e. different iterations within the same model optimization process), and the cost function for performance evaluation (i.e. h_γ in Eq. (TO)) is chosen to be the same as Example 1 in Section III-E2 which mainly penalizes the joint torques.

1) (C1) *Trajectory Optimization*: We evaluate the open-loop performance by running the full model trajectory optimization in Eq. (TO) over a range of different stride lengths and pelvis heights. As a special case, (C1) combined with (R1) corresponds to Eq. (TO) without the constraint $g_c = 0$.

2) (C2) *Simplified Cassie Simulation*: We use Drake simulation [67]. The MPC horizon is set to two footsteps, and the duration per step is fixed to 0.35 seconds which is the same as that of open-loop. Similar to the open-loop, we evaluate the performance by varying the desired stride length and pelvis height. For each desired task, we run one simulation with 12 seconds of simulation time. In each simulation, we check a set of criteria to ensure Cassie walks in a periodic gait (within a window of 4 foot steps), and then extract the actual stride length and pelvis height of that periodic gait. The evaluation is conducted for the initial model (R2), the optimal model (R3)

and also models along the model iterations from the model optimization of Section III-E2.

3) (C3) *Cassie Simulation*: The evaluation process is the same as that of simplified Cassie simulation. However, some heuristics are introduced to the MPC so that it is stabilizing. We added a double-support phase to smoothly transition between two single-support phases by linearly blending the ground forces of the two legs. This is critical for Cassie, because unloading the springs of the support leg too fast when transitioning into swing phase can cause foot oscillation and lead to bad swing foot tracking performance. The double-support phase duration was set to 0.1 seconds, and the swing phase duration was decreased to 0.3 seconds, compared to the nominal 0.35 seconds of stride duration in the trajectory optimization. Aside from the double-support phase, the rest of changes are mostly mild gain-tuning.

4) (C4) *Cassie Hardware Experiment*: We slightly tune the gains of the controller from Cassie simulation. The hardware setup is described in Section IV-C. During the experiment, we send commands to walk Cassie around and make sure that the safety hoist does not interfere with Cassie’s motion. After the experiment, we apply a moving window of 4 footsteps to extract periodic gaits for cost evaluation.

C. Comparison of Cost Landscapes

Here, we compare the cost landscape of the initial model to that of the optimal model. To compare them in the case of (C1), (C2) and (C3), we first derive the cost landscapes of both models using the cost function h_γ , and then superimpose these two cost landscapes in terms of the ratio of (R3)’s cost to (R2)’s cost. The cost landscape comparisons are shown in Fig. 6. Darker blue color corresponds to better model improvement. Green color corresponds to the tasks acquired by the optimal model (i.e. the task that the initial model cannot execute). Dark red color corresponds to the task lost after model optimization. As for the case (C4), we evaluate the cost for different stride lengths while fixing the pelvis height, and then plot the costs of both the initial model and the optimal model directly in Fig. 7.

From Fig. 6 and 7, we can see that the performance of the robot (evaluated by torque squared in this case) is better with the optimal ROM than with the initial ROM. In the open-loop, the cost improves by up to 8%, while the closed-loop can improve by up to 15%. We note that the open-loop cost improvement (Fig. 6a) is worse than that of Fig. 4, because we fix the embedding function r in this section⁷. On hardware, the performance improvement is close to 10% for walking in place. This demonstrates that the open-loop model performance is successfully transferred to the closed-loop system using the MPC, despite the modeling error in the simplified Cassie model.

Besides the cost improvement, the cost landscape plots also visualize the task regions that the ROM gains or loses after the

⁷We also added a constraint to the trajectory optimization to prevent the solver from exploiting the CoP by moving it to the edge of the support polygon.

model optimization. In the trajectory optimization case (C1)⁸, there is not a big change in the total size of the task space. In the simplified Cassie simulation (C2), the optimal model gains a decent amount of stride length at low pelvis height. For example, 19.2% growth in stride length at pelvis height = 0.7m. In Cassie simulation (C3), the optimal model also increases the overall task space size. At the normal operating pelvis heights, Cassie is capable of walking backward faster.

The task space during the model optimization is marked by a dashed box in each cost landscape in Fig. 6. This shows that the optimal model still performs well outside the training task space, and that there is not a strong correlation between the training space and cost improvement landscape, since the largest cost improvement happens at the boundary of (and outside) the training space.

We also found that the cost landscape comparison is highly dependent on the user-defined cost function h_γ . From the cost landscape in Fig. 6a, we can see that the cost improves more when the stride length decreases. However, if we heavily penalize the joint acceleration instead of the joint torque, the cost improvement increases as the stride length increases.

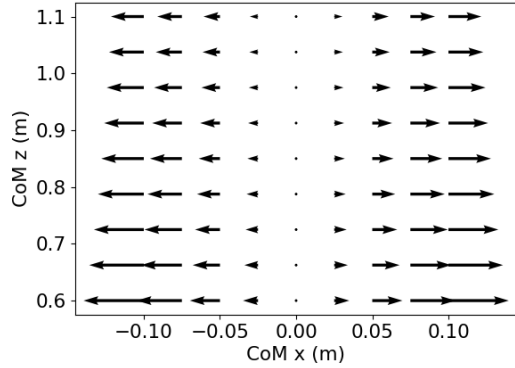
D. Optimal Robot Behaviors

In order to understand the source of the performance improvement, we look at the motion of the robot and the center of mass dynamics (the ROM dynamics g).

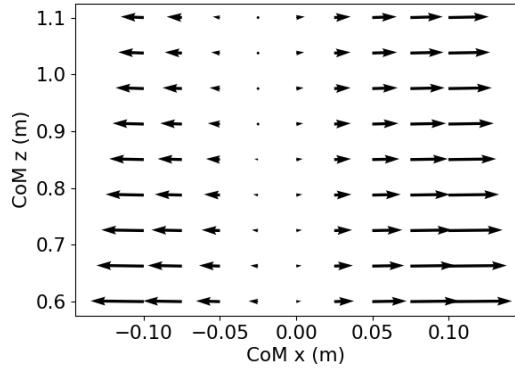
We observe in the optimal trajectories of Cassie without ROM (R1) that Cassie moves its center of pressure (CoP) closer to the rear end of the support polygon. This CoP shift also emerges in Cassie with the optimal model (R3), while the average CoP is at the center of support polygon for the initial model (R2). We observe the same CoP behavior in the simulation. On hardware, we confirm this by visualizing the projected CoM on the ground when Cassie walks in place. The CoP is close to the projected CoM, since there is little centroidal angular momentum for walking in place. The projected CoM of the hardware data indeed shifts towards the back of the support polygon when using the optimal model.

To understand why the projected CoM moves backward, we plot the ROM dynamic function g in Fig. 8 for both the initial model and the optimal model. In the case of the initial model (LIP), we know that the dynamics should be symmetrical about the z axis, specifically the acceleration should be 0 at $x = 0$ (Fig. 8a). This vector field profile, however, looks different in the case of the optimal model. As we can see from Fig. 8b, the area with near-zero acceleration shifts towards the $-x$ direction (i.e. to the back of the support polygon), and interestingly it also slightly correlates to the height of the CoM. The higher the CoM is, the further back the region of zero acceleration is. Additionally, we know that the LIP dynamics in the x - z plane is independent of the CoM y position. That is, no matter which slice of the x - z plane we take, the vector field should look identical. For the optimal model, the dynamics in the x - z plane is a function of the CoM y position. The further

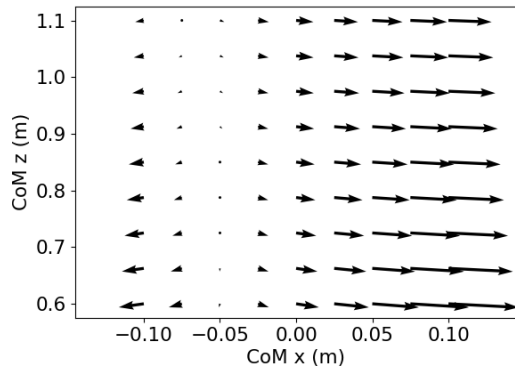
⁸In the case of (C1), there was not a clear threshold for defining the failure of a task. We picked a cost threshold at which the robot’s motion does not look abnormal.



(a) Initial model (R2). 2D slice at CoM position = 0m in y axis (when the CoM is right above the stance foot).

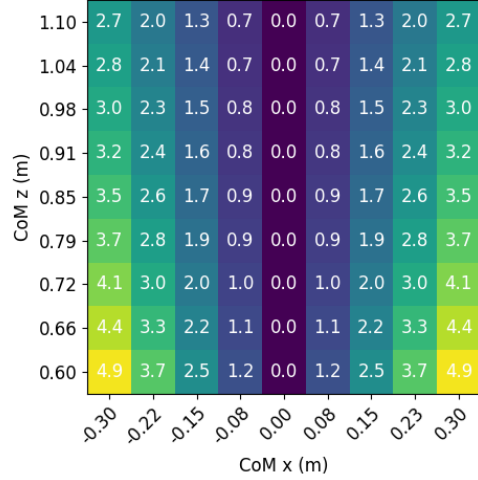


(b) Optimal model (R3). 2D slice at CoM position = 0m in y axis (when the CoM is right above the stance foot).

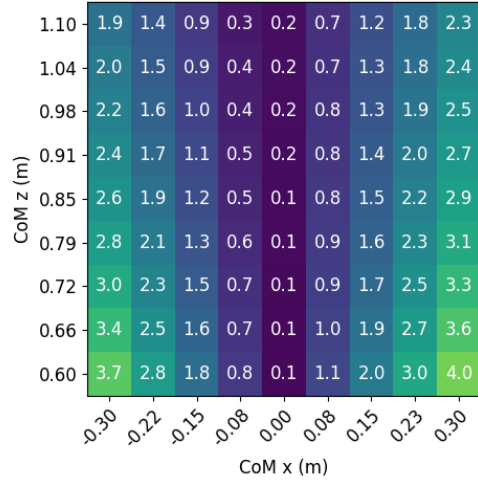


(c) Optimal model (R3). 2D slice at CoM position = -0.2m in y axis (when the CoM is to the right of the left stance foot, for example).

Fig. 8. The vector fields of the ROM dynamics g over the CoM x and z position. In this example, the dynamics is the acceleration of the CoM, which is a function of the CoM position and velocity defined in Eq. (7b). The first plot is the initial model's dynamics, while the latter two are of the optimal model at two different slices of CoM y position. In all plots, the CoM velocity is 0. We note that the size of the vectors only reflects the relative magnitude. The absolute magnitude of the vectors for the first two plots are shown in Fig. 9, although we note that the scale of the x axis is different.



(a) Initial model (R2). 2D slice at CoM position = 0m in y axis (when the CoM is right above the stance foot).



(b) Optimal model (R3). 2D slice at CoM position = 0m in y axis (when the CoM is right above the stance foot).

Fig. 9. The magnitude of ROM dynamics g over the CoM x and z position. The settings of Fig. 9a and 9b are the same as Fig. 8a and 8b, respectively.

away the CoM is from the stance foot (bigger foot spread), the further back the zero acceleration region is.

Aside from the vector field plots of the CoM dynamics, we also visualize the absolute value of the vectors in Fig. 9. We can see that the magnitude of the CoM acceleration in general becomes smaller when using the optimal model. This implies that the total ground reaction force is smaller with the optimal model, even if the robot walks at the same speed. Given the same walking speed, the robot decelerates and accelerates less in the x axis when using the optimal model (i.e., the average speed is the same, but the speed fluctuation becomes smaller after using the optimal model). We hypothesize that the decrease in ground force magnitude partially contributes to the decrease in the joint torque in the case of Cassie walking. The fact that there is less work done on the CoM during walking with the optimal ROM might have led to the decrease in torque squared which is a proxy for energy consumption.

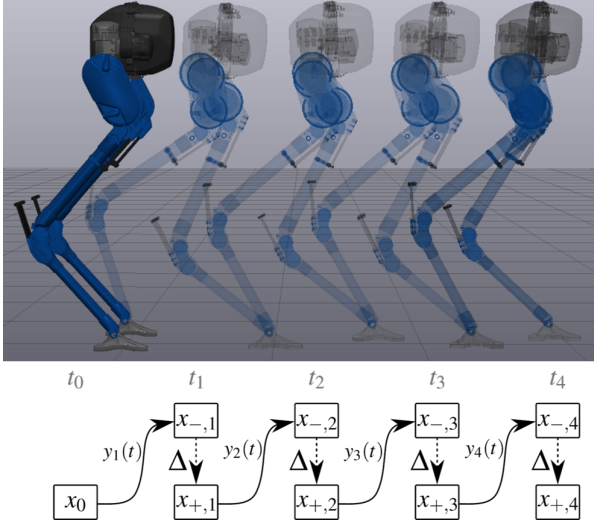


Fig. 10. An example of the real time planner in Eq. (16). Given a task of covering two meters in four steps starting from a standing pose, we rapidly plan a trajectory for the reduced-order model. The high-dimensional model is used to capture the hybrid event at stepping, as illustrated in the diagram.

The experiments in this section demonstrate two things. First, the optimal behavior along with the performance (cost) can be transferred from the open-loop training (left side of Fig. 1) to a closed-loop system (right side of Fig. 1). Second, the optimal reduced-order model improves the real Cassie’s performance, while the low dimensionality permits real time planning application.

VI. MPC FOR A GENERAL ROM

In our experimental work, we focused on a limited class of ROM’s with a known embedding, since they enabled the highest-speed computation and we could rely on the physical interoperability of the ROM to guide the planner. Here, we give an approach for a general ROM defined by Eq. (6), and we must expose some full-order states to provide the same meaning to the resulting plan.

A. Hybrid Nature of the Robot Dynamics

Shown in Eq. (2), the dynamics of the full model is hybrid – it contains both the continuous-time dynamics and discrete-time dynamics due to the foot collision. In contrast, many existing reduced-order models assume zero impacts at foot touchdown. This is partially due to the fact that the exact embedding of a reduced-order discrete dynamics does not always exist. For example, we could have two pre-impact states x of the full model that correspond to the same reduced-order states, but the post-impact states of the full model map to two different reduced-order states. In this case, the reduced-order discrete dynamics is not an ordinary (single-valued) function. Therefore, in order to capture the exact full impact dynamics in the planner, it is necessary to mix the reduced-order model with the discrete dynamics from the full-order model. We note that the traditional approaches to reduced-order planning and embedding must also grapple with approximations of the impact event.

In addition to the issue above, the mix of reduced- and full-order models also seems necessary if we do not retain the physical interpretability of the embedding r when planning for the optimal footstep locations in the planner. This results in a low-dimensional trajectory optimization problem, a search for $y_j(t)$ and $\tau_j(t)$, with additional decision variables $x_{-,j}, x_{+,j}$, representing the pre- and post-impact full-order states. The index j refers to the j th stride. The constraints relating the reduced-order state to the full-order model and the impact dynamics are

$$y_j(t_j) = r(q_{-,j}; \theta_e), \quad \dot{y}_j(t_j) = \frac{\partial r(q_{-,j}; \theta_e)}{\partial q_{-,j}} \dot{q}_{-,j},$$

$$y_{j+1}(t_j) = r(q_{+,j}; \theta_e), \quad \dot{y}_{j+1}(t_j) = \frac{\partial r(q_{+,j}; \theta_e)}{\partial q_{+,j}} \dot{q}_{+,j}, \quad (15)$$

and $C_{\text{hybrid}}(x_{-,j}, x_{+,j}, \Lambda_j) \leq 0,$

where t_j ’s are the impact times (ending the j th stride), C_{hybrid} represents the hybrid guard S and the impact mapping Δ without left-right leg alternation⁹.

B. Planning with ROM and Full-order Impact Dynamics

Similar to Section IV, we formulate a reduced-order trajectory optimization problem to walk n_s strides. However, we replace the discrete footstep inputs T_{fp} with the full robot states $x_{-,j}$ and $x_{+,j}$. To improve readability, we stack decision variables into bigger vectors $T = [\tau_1, \dots, \tau_n] \in \mathbb{R}^{n_{\tau}n}$ and $X = [x_{-,1}, \dots, x_{-,n_s}, x_{+,1}, \dots, x_{+,n_s}] \in \mathbb{R}^{2n_xn_s}$.

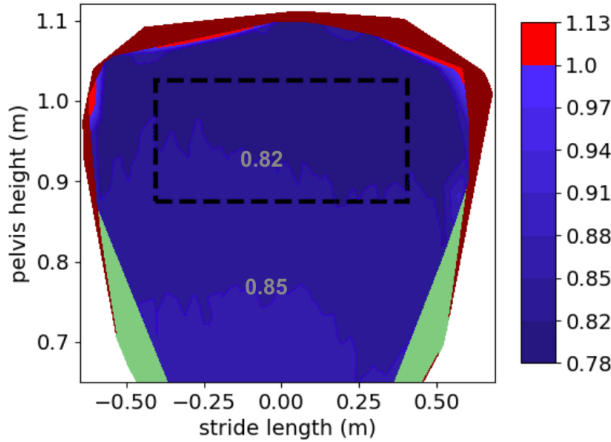
Costs are nominally expressed in terms of $[y, \dot{y}]$ and τ , though the pre- and post-impact full-order states can also be used to represent goal locations. In addition to the constraints in Eq. (15), we impose constraints $C_{\text{kinematics}}(X) \leq 0$ on the full model’s kinematics such that the solution obeys joint limits, stance foot stays fixed during the stance phase, and legs do not collide with each other.

The planning problem with the general ROM is

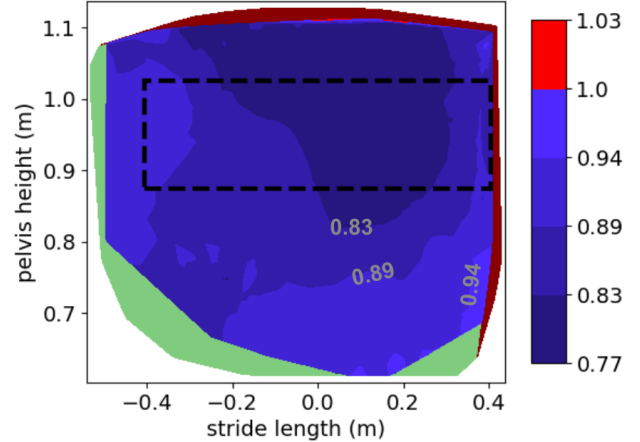
$$\begin{aligned} \min_w \quad & \|T\|_{W_T}^2 + \|Z - Z_{\text{reg}}\|_{W_Z}^2 + \|X - X_{\text{reg}}\|_{W_X}^2 \\ \text{s.t.} \quad & \text{Reduced-order dynamics (Eq. (7b)),} \\ & \text{Hybrid constraints (Eq. (15)),} \\ & C_{\text{kinematics}}(X) \leq 0, \\ & x_0 = \text{current feedback full-order state,} \end{aligned} \quad (16)$$

where $w = [Z, T, \delta_1, \dots, \delta_{n_s-1}, x_0, X, \Lambda_1, \dots, \Lambda_{n_s}] \in \mathbb{R}^{n_w}$, $W_{(\cdot)}$ ’s are the weights of the norms, Z_{reg} is the regularization state for the reduced model, and X_{reg} is the regularization state for the full state and contains the goal location of the robot. After solving Eq. (16), we reconstruct the desired ROM trajectory $y_d(t)$ from the optimal solution Z^* . Different from Section IV, the optimal solution w^* here also contains the desired full-order states X^* at impact events, from which we derive not only the desired swing foot stepping locations but also the desired trajectories for joints such as swing hip yaw and swing toe joint. Additionally, since there are full states in the planner, we can send the velocity command of pelvis yaw directly to the ROM planner.

⁹The impact mapping Δ can be simplified to identity if we assume no impact (i.e. swing foot touchdown velocity is 0 in the vertical axis).



(a) Trajectory optimization with the simplified Cassie model, (C1).



(b) Simplified Cassie simulation, (C2).

Fig. 11. The same plots as those in Fig. 6a and 6b except that here we allow the solver to exploit the model optimization problem by moving the robot's CoP arbitrarily close to the edge of the support polygon. We can see that the resultant cost improvement is about twice of that of Fig. 6. However, it is hard to stabilize around the planned trajectories of this optimal model on hardware.

Fig. 10 visualizes the pre-impact states in the case where the robot walks two meters with four strides, connected by the hybrid events and continuous low-dimensional trajectories $y_j(t)$. Although there is no guarantee that the planned trajectories $y_j(t)$ are feasible for the full model except those at the hybrid events, we were able to retrieve $q(t)$ from $y_j(t)$ through inverse kinematics, meaning the embedding existed empirically. We note that classical models like LIP also provide no guarantees [73]. For instance, there is no constraint on leg lengths in the ROM which could lead to kinematic infeasibility. The formulation in Eq. (16) preserves an exact representation of the hybrid dynamics, but results in a significantly reduced optimization problem.

C. Implementation and Experiments

We implement an MPC using Eq. (16) for both simulation and hardware experiments (the hardware setup is the same as Section IV-C). In simulation, we were able to transfer the open-loop performance to closed-loop performance with this new MPC. However, on hardware, the off-the-shelf solvers IPOPT and SNOPT were not capable of solving the planning problem in Eq. (16) fast enough or well enough to enable a high-performance real time MPC¹⁰. With IPOPT, the planner simply did not run fast enough. With SNOPT, even though the solve time can be decreased down to 30ms with loose optimality tolerance and constraint tolerance, we sacrificed the solution quality too much to achieve big stride length on Cassie. Nonetheless, we believe this to be a matter of software engineering. Boston Dynamics has empirically shown the value of well-engineered custom solvers with their success in the nonlinear MPC with the centroidal momentum model and full robot kinematics [74].

¹⁰Currently Drake's implementation of multibody kinematics and dynamics evaluation is slow with automatic differentiation, so we have to numerically differentiate the nonlinear constraint in our MPC implementation, which is computationally expensive.

VII. DISCUSSION

A. Performance Gap

The proposed approach to model optimization uses full-model trajectory optimization. This has a few advantages. First, it allows us to embed the reduced-order model into the full model exactly via constraints. Second, it is more sample efficient than the approaches in reinforcement learning (such as [31]). However, using trajectory optimization leaves a potential performance gap between the offline training and online deployment, because trajectory optimization is an open-loop optimal control method which does not consider any controller heuristics by default. For instance, our walking controller constructs the swing foot trajectory with cubic splines, and we found the open-loop performance can be transferred to the closed-loop better after we add this cubic spline heuristic as a constraint in the trajectory optimization problem.

While we have seen the performance of the robot improve, we also observed that the solver would exploit any degree of freedom of the input and state variables during the model training stage. For example, the center of pressure turned out to play an important role in improving the performance (reducing joint torques) of Cassie in Section V. If we had not regularized the CoP (or the CoM motion) during the model optimization stage, the solver would have moved the CoP all the way to the edge of the support polygon. Although this exploitation can lead to a much bigger cost improvement as shown in Fig. 11, it also destroys the robustness of the model. Under hardware noise and model uncertainty, tracking the planned trajectories of this optimal model cannot stabilize the robot well, and thus the performance cannot be transferred to the hardware. One principled way of fixing this issue is to optimize the robustness of the trajectory alongside the user-defined cost function [75], [76].

For the general optimal ROM MPC in Section VI, one place where the performance gap can enter is the choice of the cost function in Eq. (16). In our past experiments, we

simply ran a full model trajectory optimization and used this optimal trajectory for the regularization term in Eq. (16). It worked well, although there was a slight improvement drop. To mitigate the gap, one could try inverse optimal control to learn the MPC cost function given data from the full model trajectory optimization.

Since our robot has one-DOF underactuation caused by line feet design, it is not trivial to track the desired trajectory of the reduced-order model within the continuous phase of hybrid dynamics. We noticed in the experiment that there was a noticeable performance difference between whether or not we tracked the first element of the desired ROM trajectory. Therefore, we conjecture that if we use a robot with a finite size of feet, we could translate the open-loop performance to the closed-loop performance better and more easily.

Lastly, we found that empirically it is easier to transfer model performance from open-loop to closed-loop when we fix embedding function r , although the open-loop performance improvement is usually much bigger (sometimes near full-model's performance) when we optimize both the embedding function r and dynamics g . As a concrete example, in some model optimization instances the optimal ROM position y can be insensitive to the change of CoM position, which makes it difficult to servo the CoM height. In the worst case, this insensitivity could lead to substantial CoM height movement and instability of the closed-loop system.

B. Physical Interpretability

While we parametrized the embedding function r with monomials in the examples, we could have also parameterized it in a physically-interpretable way by providing more structures. As an example, we can initialize the ROM to the SLIP model and parametrize the spring stiffness in terms of center of mass velocities. One downside of hand-crafted structures is that we limit the ROM space that the algorithm optimizes over, which in general sacrifices the maximum potential performance improvement.

C. Generality of Our Framework

This paper focuses on applying the optimal ROMs to Cassie, but the approach is broader than Cassie and might achieve greater performance benefits on other robots where the LIP is worse. For example, we saw more than 75% of cost reduction for the five-link planar robot in our prior work [33]. Furthermore, the framework itself is agnostic to types of robots and tasks. This has implications all over robotics, given the need for computational efficiency and the prevalence of reduced-order models in locomotion and manipulation.

VIII. CONCLUSION

In this work, we directly optimized the reduced-order models which can be used in an online planner that achieved performance higher than that of the traditional physical models. We formulated a bilevel optimization problem and presented an efficient algorithm that leverages the problem structure. Examples showed improvements up to 38% depending on

the task difficulty and the performance metric. The optimal reduced-order models are more permissive and capable of higher performance, while remaining low dimensional. We also designed two MPC's for the optimal reduced-order models which enable Cassie to accomplish tasks with better performance. In the hardware experiment, the optimal ROM showed 10% of improvement on Cassie, and we investigated the source of performance gains for this particular model. We demonstrated that the use of ROM greatly reduces planning speed, and that the optimized ROM improves the performance of the robot beyond the traditional ROM's.

Although the model optimization approach presented in this paper has the advantage of optimizing models agnostic to low-level controllers, it does not guarantee that the performance improvements from these optimal models can be transferred to the robot via a feedback controller as discussed in Section VII-A. One ongoing work is to fix the above issue by optimizing the model in a closed-loop fashion, so that the model optimization accounts for the controller heuristics and maintains the closed-loop stability. This would also potentially ease the process of realizing the optimal model performance on hardware. Additionally, discussed in Section VI-A, an approximation is necessary if we were to find a low dimensional representation of the full-order impact dynamics. In this work, we only circumvented the hybrid problem by either using a physically-interpretable ROM or mixing the full impact dynamics with the FOM. Finding an optimal low-dimensional discrete dynamics for a robot still remains an open question.

ACKNOWLEDGEMENTS

We thank Wanxin Jin for discussions on Envelope Theorem and approaches to differentiating an optimization problem. Toyota Research Institute provided funds to support this work.

APPENDIX A HEURISTICS IN TRAJECTORY OPTIMIZATION

Solving the trajectory optimization problem in Eq. (4) or (TO) for a high-dimensional robot is hard, since the problem is nonlinear and of large scale. Even although there are off-the-shelf solvers such as IPOPT [71] and SNOPT [66] designed to solve large-scale nonlinear optimization problem, it is often impossible get a good optimal solution without any heuristics. In this section, we will talk from our experience about the heuristics that might help to solve the problem faster and also find a more optimal solution.

Let the nonlinear problem be

$$\begin{aligned} \min_w \quad & \tilde{h}(w) \\ \text{s.t.} \quad & \tilde{f}(w) \leq 0 \end{aligned} \tag{17}$$

where w contains all decision variables, \tilde{h} is the cost function, and \tilde{f} is the constraint function. It turned out that scaling either w , \tilde{h} or \tilde{f} could help to improve the condition of the problem.

- w : Sometimes the decision variables are in different units and can take values of different orders. For example, joint angles of Cassie are roughly less than 1 (rad), while its contact forces are usually larger than 100 (N). In this case,

we can scale w by some factor s , such that the decision variables of the new problem are $w_{scaled,i} = s_i w_i$ for $i = 1, 2, \dots, n_w$. After the problem is solved, we scale the optimal solution of the new problem back by $w_i^* = \frac{1}{s_i} w_{scaled,i}^*$.

- f : The constraints \tilde{f} can take various units just like w . Similarly, we can scale each constraint individually. Note that scaling constraints affects how well the original constraints are satisfied, so one should make sure that the constraint tolerance is still meaningful.
- \tilde{h} : In theory, scaling the cost does not affect the optimal solution. However, it does matter in the solver's algorithm. It is desirable to scale the cost so that it is not larger than 1 around the area of interest.

For more detail about scaling, we refer the readers to Chapter 8.4 and Chapter 8.7 of [77]. In addition to scaling the problem, the following heuristics could also be helpful:

- Provide the solver with a good initial guess.
- Add small randomness to the initial guess: This helps to avoid singularities.
- Add regularization terms to the cost function: This could remove local minima in the cost landscape and can also speed up the solve time. Adding regularization terms is similar to the traditional reward shaping of Reinforcement Learning [78] and the policy-regularized MPC [79].
- Add intermediate variables (also called slack variables [80]): This can sometimes improve the condition number of the constraint gradients with respect to decision variables. One example of this is reformulating the trajectory optimization problem based on the single shooting method into that based on the multiple shooting method by introducing state variables [81].
- Use solver's internal scaling option: In the case of SNOPT [82], we found setting *Scale option* to 2 helps to find an optimal solution of better quality. Note that this option increases the solve time and demands a good initial guess to the problem.

APPENDIX B MIRRORED REDUCED-ORDER MODEL

A. Model definition

The model representation in Eq. (7) could be dependent on the side of the robot. For example, when using the LIP model as the ROM, we might choose the generalized position of the model y to be the CoM position relative to the left foot (instead of the right foot). In this case, we need to find the reduced-order model for the right support phase of the robot. Fortunately, we can derive this ROM by mirroring the robot configuration q about its sagittal plane (Fig. 12) and reusing the ROM of the left support phase. We refer to this new ROM as the *mirrored reduced-order model*.

Let q_m and v_m be the generalized position and velocity of the “mirrored robot”, shown in Fig. 12. Mathematically, the mirrored ROM μ_m is

$$\mu_m \triangleq (r_m, g), \quad (18)$$

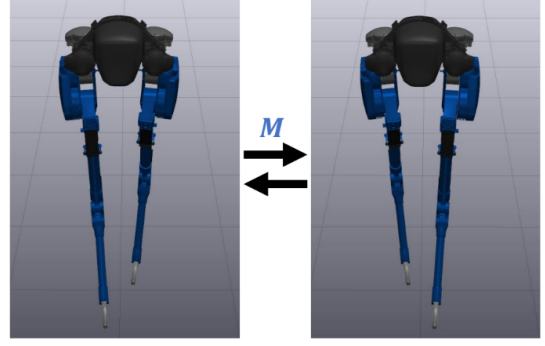


Fig. 12. The mirror function M mirrors the robot configuration about the sagittal plane. This function is necessary in planning and control when the embedding function (Eq. (7a)) of the reduced-order model only represents one side of the robot. For example, the embedding function of the LIP model was chosen to be the CoM relative to the left foot (and not the right foot).

with

$$y_m = r_m(q) = r(q_m) = r(M(q)), \quad (19a)$$

$$\dot{y}_m = g(y_m, \dot{y}_m, \tau), \quad (19b)$$

where r_m is the embedding function of the mirror model, and M is the mirror function such that $q_m = M(q)$ and $q = M(q_m)$. We note that the two models, in Eq. (6) and (18), share the same dynamics function g .

B. Time derivatives of the embedding function

Feedback control around a desired trajectory often requires the first and the second time derivatives information. Here, we derive these quantities for the mirrored ROM in terms of the original embedding function r in Eq. (7a) and its derivatives.

1) \dot{y}_m : Let J_m be the Jacobian of the mirrored model embedding r_m with respect to the robot configuration q , such that

$$\dot{y}_m = J_m \dot{q}. \quad (20)$$

The time derivatives of y_m is

$$\ddot{y}_m = \frac{\partial r(M(q))}{\partial M(q)} \frac{\partial M(q)}{\partial q} \dot{q} = J(q_m) \frac{\partial M(q)}{\partial q} \dot{q} = J(q_m) \dot{q}_m \quad (21)$$

where $J(q_m)$ is the Jacobian of the original model embedding r evaluated with q_m . From Eq. (20) and (21), we derive

$$J_m = J(q_m) \frac{\partial M(q)}{\partial q} \quad (22)$$

where $\frac{\partial M(q)}{\partial q}$ is a matrix which contains only 0, 1, and -1.

2) \ddot{y}_m : The i -th element of \ddot{y}_m is

$$\begin{aligned} \ddot{y}_{m,i} &= \frac{d}{dt} \left(\frac{\partial r_i(q_m)}{\partial q_m} \dot{q}_m \right) = \frac{d}{dt} \sum_j \frac{\partial r_i(q_m)}{\partial q_{m,j}} \dot{q}_{m,j} \\ &= \sum_j \frac{d}{dt} \left(\frac{\partial r_i(q_m)}{\partial q_{m,j}} \right) \dot{q}_{m,j} + \sum_j \frac{\partial r_i(q_m)}{\partial q_{m,j}} \frac{d}{dt} (\dot{q}_{m,j}) \\ &= \sum_{jk} \frac{\partial^2 r_i(q_m)}{\partial q_{m,j} \partial q_{m,k}} \dot{q}_{m,j} \dot{q}_{m,k} + \frac{\partial r_i(q_m)}{\partial q_m} \frac{d}{dt} (\dot{q}_m). \end{aligned}$$

where r_i is the i -th element of the embedding function. The above equation can be expressed in the vector-matrix form

$$\begin{aligned}\ddot{y}_m &= \dot{q}_m^T \nabla^2 r(q_m) \dot{q}_m + J(q_m) \ddot{q}_m \\ &= \dot{J}(q_m, v_m) \dot{q}_m + J(q_m) \ddot{q}_m \\ &= \dot{J}(q_m, v_m) \dot{q}_m + J_m \dot{v} \quad (\because \text{Eq. (22)})\end{aligned}\quad (23)$$

where $\dot{J}(q_m, v_m)$ is the time derivatives of the J (of the original model) evaluated with the mirrored position q_m and velocity v_m .

C. Examples

In the ROM trajectory planner of Section VI, Eq. (15) uses Eq. (7a) and its derivatives for the left support phase, and uses Eq. (19a) and (21) for the right support phase. As for the dynamics constraint during the continuous phase, we can use Eq. (7b) for both phases, because the original model and the mirrored model share the same dynamics function.

In the operational space control of Section IV-B, Eq. (14b) uses Eq. (19a), (21), (22) and (23) for the mirrored reduced-order model.

REFERENCES

- [1] P. M. Wensing, M. Posa, Y. Hu, A. Escande, N. Mansard, and A. Del Prete, “Optimization-based control for dynamic legged robots,” *arXiv preprint arXiv:2211.11644*, 2022.
- [2] E. R. Westervelt, J. W. Grizzle, and D. E. Koditschek, “Hybrid zero dynamics of planar biped walkers,” *IEEE transactions on automatic control*, vol. 48, no. 1, pp. 42–56, 2003.
- [3] H. Zhao, A. Hereid, W.-l. Ma, and A. D. Ames, “Multi-contact bipedal robotic locomotion,” *Robotica*, vol. 35, no. 5, pp. 1072–1106, 2017.
- [4] J. Reher, E. A. Cousineau, A. Hereid, C. M. Hubicki, and A. D. Ames, “Realizing dynamic and efficient bipedal locomotion on the humanoid robot durus,” in *2016 IEEE International Conference on Robotics and Automation (ICRA)*, pp. 1794–1801, IEEE, 2016.
- [5] D. E. Orin and A. Goswami, “Centroidal momentum matrix of a humanoid robot: Structure and properties,” in *2008 IEEE/RSJ International Conference on Intelligent Robots and Systems*, pp. 653–659, IEEE, 2008.
- [6] P. M. Wensing and D. E. Orin, “Improved computation of the humanoid centroidal dynamics and application for whole-body control,” *International Journal of Humanoid Robotics*, vol. 13, no. 01, p. 1550039, 2016.
- [7] S. Kajita and K. Tani, “Study of dynamic biped locomotion on rugged terrain-derivation and application of the linear inverted pendulum mode,” vol. 2, pp. 1405–1411, IEEE International Conference on Robotics and Automation (ICRA), 1991.
- [8] S. Kajita, F. Kanehiro, K. Kaneko, K. Yokoi, and H. Hirukawa, “The 3D linear inverted pendulum mode: a simple modeling for a biped walking pattern generation,” pp. 239–246, IEEE International Conference on Intelligent Robots and Systems (IROS), 2001.
- [9] R. Blickhan, “The spring-mass model for running and hopping,” *Journal of biomechanics*, vol. 22, no. 11-12, pp. 1217–1227, 1989.
- [10] X. Xiong and A. D. Ames, “Dynamic and versatile humanoid walking via embedding 3d actuated slip model with hybrid lip based stepping,” *IEEE Robotics and Automation Letters*, vol. 5, no. 4, pp. 6286–6293, 2020.
- [11] X. Xiong, J. Reher, and A. Ames, “Global position control on under-actuated bipedal robots: Step-to-step dynamics approximation for step planning,” *arXiv preprint arXiv:2011.06050*, 2020.
- [12] M. Kasaie, A. Ahmadi, N. Lau, and A. Pereira, “A robust model-based biped locomotion framework based on three-mass model: From planning to control,” in *2020 IEEE International Conference on Autonomous Robot Systems and Competitions (ICARSC)*, pp. 257–262, IEEE, 2020.
- [13] T. Takenaka, T. Matsumoto, and T. Yoshiike, “Real time motion generation and control for biped robot-1 st report: Walking gait pattern generation,” in *2009 IEEE/RSJ International Conference on Intelligent Robots and Systems*, pp. 1084–1091, IEEE, 2009.
- [14] T. Sato, S. Sakaino, and K. Ohnishi, “Real-time walking trajectory generation method with three-mass models at constant body height for three-dimensional biped robots,” *IEEE transactions on industrial electronics*, vol. 58, no. 2, pp. 376–383, 2010.
- [15] S. Shimmyo, T. Sato, and K. Ohnishi, “Biped walking pattern generation by using preview control based on three-mass model,” *IEEE transactions on industrial electronics*, vol. 60, no. 11, pp. 5137–5147, 2012.
- [16] S. M. KASAIE, N. LAU, and A. PEREIRA, “A reliable hierarchical omnidirectional walking engine for a bipedal robot by using the enhanced lip plus flywheel,” in *Human-Centric Robotics: Proceedings of CLAWAR 2017: 20th International Conference on Climbing and Walking Robots and the Support Technologies for Mobile Machines*, pp. 399–406, World Scientific, 2018.
- [17] S. Faraji and A. J. Ijspeert, “3lp: A linear 3d-walking model including torso and swing dynamics,” *the international journal of robotics research*, vol. 36, no. 4, pp. 436–455, 2017.
- [18] M. Chignoli, D. Kim, E. Stanger-Jones, and S. Kim, “The mit humanoid robot: Design, motion planning, and control for acrobatic behaviors,” *arXiv preprint arXiv:2104.09025*, 2021.
- [19] A. Shaiju and I. R. Petersen, “Formulas for discrete time lqr, lqg, leqg and minimax lqg optimal control problems,” *IFAC Proceedings Volumes*, vol. 41, no. 2, pp. 8773–8778, 2008.
- [20] C. E. Garcia, D. M. Pretti, and M. Morari, “Model predictive control: Theory and practice—a survey,” *Automatica*, vol. 25, no. 3, pp. 335–348, 1989.
- [21] F. Borrelli, A. Bemporad, and M. Morari, *Predictive control for linear and hybrid systems*. Cambridge University Press, 2017.
- [22] Y. Gong and J. Grizzle, “Zero dynamics, pendulum models, and angular momentum in feedback control of bipedal locomotion,” *arXiv preprint arXiv:2105.08170*, 2021.
- [23] G. Gibson, O. Dosunmu-Ogunbi, Y. Gong, and J. Grizzle, “Terrain-aware foot placement for bipedal locomotion combining model predictive control, virtual constraints, and the alip,” *arXiv preprint arXiv:2109.14862*, 2021.
- [24] H. Dai, A. Valenzuela, and R. Tedrake, “Whole-body Motion Planning with Centroidal Dynamics and Full Kinematics,” *IEEE-RAS International Conference on Humanoid Robots*, 2014.
- [25] A. Herzog, S. Schaal, and L. Righetti, “Structured contact force optimization for kino-dynamic motion generation,” in *2016 IEEE/RSJ International Conference on Intelligent Robots and Systems (IROS)*, pp. 2703–2710, IEEE, 2016.
- [26] P. Marion and the team, “Flipping the script with atlas.” <https://blog.bostondynamics.com/flipping-the-script-with-atlas>.
- [27] M. Posa, T. Koolen, and R. Tedrake, “Balancing and Step Recovery Capturability via Sums-of-Squares Optimization,” in *Robotics: Science and Systems*, 2017.
- [28] T. Koolen, M. Posa, and R. Tedrake, “Balance control using center of mass height variation: limitations imposed by unilateral contact,” in *Humanoid Robots (Humanoids), 2016 IEEE-RAS 16th International Conference on*, pp. 8–15, IEEE, 2016.
- [29] H. Li, R. J. Frei, and P. M. Wensing, “Model hierarchy predictive control of robotic systems,” *IEEE Robotics and Automation Letters*, vol. 6, no. 2, pp. 3373–3380, 2021.
- [30] J. Norby, A. Tajbakhsh, Y. Yang, and A. M. Johnson, “Adaptive complexity model predictive control,” *arXiv preprint arXiv:2209.02849*, 2022.
- [31] A. Pandala, R. T. Fawcett, U. Rosolia, A. D. Ames, and K. A. Hamed, “Robust predictive control for quadrupedal locomotion: Learning to close the gap between reduced-and full-order models,” *IEEE Robotics and Automation Letters*, vol. 7, no. 3, pp. 6622–6629, 2022.
- [32] G. G. R. P. M. Chen, Yu-Ming Nelson, and J. Pratt, “Angular center of mass for humanoid robots,” *arXiv preprint arXiv:2210.08111*, 2022.
- [33] Y.-M. Chen and M. Posa, “Optimal reduced-order modeling of bipedal locomotion,” in *2020 IEEE International Conference on Robotics and Automation (ICRA)*, pp. 8753–8760, IEEE, 2020.
- [34] R. J. Full and D. E. Koditschek, “Templates and anchors: neuromechanical hypotheses of legged locomotion on land,” *The Journal of Experimental Biology*, vol. 202, pp. 3325–3332, 1999.
- [35] U. Saranli, M. Buehler, and D. E. Koditschek, “RHex: A Simple and Highly Mobile Hexapod Robot,” *The International Journal of Robotics Research*, vol. 20, pp. 616–631, jul 2001.
- [36] M. H. Raibert, H. B. Brown, and M. Chepponis, “Experiments in Balance with a 3D One-Legged Hopping Machine,” *The International Journal of Robotics Research*, vol. 3, pp. 75–92, jun 1984.
- [37] M. Garcia, A. Chatterjee, A. Ruina, and M. Coleman, “The Simplest Walking Model: Stability, Complexity, and Scaling,” *Journal of Biomechanical Engineering*, vol. 120, p. 281, apr 1998.

[38] A. L. Schwab and M. Wisse, "BASIN OF ATTRACTION OF THE SIMPLEST WALKING MODEL," in *ASME 2001 Design Engineering Technical Conferences and Computers and Information in Engineering Conference*, 2001.

[39] K. Byl and R. Tedrake, "Metastable Walking Machines," *The International Journal of Robotics Research*, vol. 28, pp. 1040–1064, aug 2009.

[40] C. Oguz Saglam and K. Byl, "Robust Policies via Meshing for Metastable Rough Terrain Walking," in *Robotics: Science and Systems*, 2014.

[41] M. Kelly and A. Ruina, "Non-linear robust control for inverted-pendulum 2D walking," in *2015 IEEE International Conference on Robotics and Automation (ICRA)*, pp. 4353–4358, IEEE, may 2015.

[42] T. Koolen, T. de Boer, J. Rebula, A. Goswami, and J. Pratt, "Capturability-based analysis and control of legged locomotion, Part 1: Theory and application to three simple gait models," *The International Journal of Robotics Research*, vol. 31, no. 9, pp. 1094–1113, 2012.

[43] J. Pratt, J. Carff, S. Drakunov, and A. Goswami, "Capture point: A step toward humanoid push recovery," in *2006 6th IEEE-RAS international conference on humanoid robots*, pp. 200–207, IEEE, 2006.

[44] B. Wie and P. M. Barba, "Quaternion feedback for spacecraft large angle maneuvers," *Journal of Guidance, Control, and Dynamics*, vol. 8, no. 3, pp. 360–365, 1985.

[45] Y. Hurmuzlu and D. B. Marghitu, "Rigid body collisions of planar kinematic chains with multiple contact points," *The international journal of robotics research*, vol. 13, no. 1, pp. 82–92, 1994.

[46] J. W. Grizzle, C. Chevallereau, R. W. Sinnet, and A. D. Ames, "Models, feedback control, and open problems of 3d bipedal robotic walking," *Automatica*, vol. 50, no. 8, pp. 1955–1988, 2014.

[47] A. Hereid, O. Harib, R. Hartley, Y. Gong, and J. W. Grizzle, "Rapid bipedal gait design using c-frost with illustration on a cassie-series robot," *arXiv preprint arXiv:1807.06614*, 2018.

[48] J. T. Betts, *Practical Methods for Optimal Control Using Nonlinear Programming*. SIAM Advances in Design and Control, Society for Industrial and Applied Mathematics, 2001.

[49] M. Posa, C. Cantu, and R. Tedrake, "A Direct Method for Trajectory Optimization of Rigid Bodies Through Contact," *The International Journal of Robotics Research*, vol. 33, pp. 69–81, jan 2013.

[50] M. Posa, S. Kuindersma, and R. Tedrake, "Optimization and stabilization of trajectories for constrained dynamical systems," in *2016 IEEE International Conference on Robotics and Automation*, vol. 2016-June, (Stockholm, Sweden), pp. 1366–1373, may 2016.

[51] J. Bracken and J. T. McGill, "Mathematical programs with optimization problems in the constraints," *Operations Research*, vol. 21, no. 1, pp. 37–44, 1973.

[52] L. Franceschi, P. Frasconi, S. Salzo, R. Grazzi, and M. Pontil, "Bilevel programming for hyperparameter optimization and meta-learning," in *International Conference on Machine Learning*, pp. 1568–1577, PMLR, 2018.

[53] A. Rajeswaran, I. Mordatch, and V. Kumar, "A game theoretic framework for model based reinforcement learning," in *International conference on machine learning*, pp. 7953–7963, PMLR, 2020.

[54] W. Jin, T. D. Murphey, D. Kulic, N. Ezer, and S. Mou, "Learning from sparse demonstrations," *IEEE Transactions on Robotics*, 2022.

[55] S. Pfrommer, M. Halm, and M. Posa, "Contactnets: Learning discontinuous contact dynamics with smooth, implicit representations," in *Conference on Robot Learning*, pp. 2279–2291, PMLR, 2021.

[56] A. Sinha, P. Malo, and K. Deb, "A review on bilevel optimization: from classical to evolutionary approaches and applications," *IEEE Transactions on Evolutionary Computation*, vol. 22, no. 2, pp. 276–295, 2017.

[57] K. Hatz, J. P. Schloeder, and H. G. Bock, "Estimating parameters in optimal control problems," *SIAM Journal on Scientific Computing*, vol. 34, no. 3, pp. A1707–A1728, 2012.

[58] C. Shi, J. Lu, and G. Zhang, "An extended kuhn–tucker approach for linear bilevel programming," *Applied Mathematics and Computation*, vol. 162, no. 1, pp. 51–63, 2005.

[59] H. W. Kuhn and A. W. Tucker, "Nonlinear programming," in *Proceedings of the Second Berkeley Symposium on Mathematical Statistics and Probability*, (Berkeley, Calif.), pp. 481–492, University of California Press, 1951.

[60] W. Jin, Z. Wang, Z. Yang, and S. Mou, "Pontryagin differentiable programming: An end-to-end learning and control framework," *Advances in Neural Information Processing Systems*, vol. 33, pp. 7979–7992, 2020.

[61] J. Domke, "Generic methods for optimization-based modeling," in *Artificial Intelligence and Statistics*, pp. 318–326, PMLR, 2012.

[62] N. Das, S. Bechtle, T. Davchev, D. Jayaraman, A. Rai, and F. Meier, "Model-based inverse reinforcement learning from visual demonstrations," in *Conference on Robot Learning*, pp. 1930–1942, PMLR, 2021.

[63] S. G. Krantz and H. R. Parks, *The implicit function theorem: history, theory, and applications*. Springer Science & Business Media, 2002.

[64] S. Afriat, "Theory of maxima and the method of lagrange," *SIAM Journal on Applied Mathematics*, vol. 20, no. 3, pp. 343–357, 1971.

[65] A. Takayama and T. Akira, *Mathematical economics*. Cambridge university press, 1985.

[66] P. E. Gill, W. Murray, and M. A. Saunders, "Snopt: An sqp algorithm for large-scale constrained optimization," *SIAM review*, vol. 47, no. 1, pp. 99–131, 2005.

[67] R. Tedrake and the Drake Team Development, "Drake: A planning, control, and analysis toolbox for nonlinear dynamical systems," 2016.

[68] L. Sentis and O. Khatib, "Control of free-floating humanoid robots through task prioritization," in *Proceedings of the 2005 IEEE International Conference on Robotics and Automation*, pp. 1718–1723, IEEE, 2005.

[69] P. M. Wensing and D. E. Orin, "Generation of dynamic humanoid behaviors through task-space control with conic optimization," in *2013 IEEE International Conference on Robotics and Automation*, pp. 3103–3109, IEEE, 2013.

[70] A. S. Huang, E. Olson, and D. C. Moore, "Lcm: Lightweight communications and marshalling," in *2010 IEEE/RSJ International Conference on Intelligent Robots and Systems*, pp. 4057–4062, IEEE, 2010.

[71] A. Wächter and L. T. Biegler, "On the implementation of an interior-point filter line-search algorithm for large-scale nonlinear programming," *Mathematical programming*, vol. 106, no. 1, pp. 25–57, 2006.

[72] J. Reher, W.-L. Ma, and A. D. Ames, "Dynamic walking with compliance on a cassie bipedal robot," in *2019 18th European Control Conference (ECC)*, pp. 2589–2595, IEEE, 2019.

[73] A. Iqbal, S. Veer, and Y. Gu, "Drs-lip: Linear inverted pendulum model for legged locomotion on dynamic rigid surfaces," *arXiv preprint arXiv:2202.00151*, 2022.

[74] "2022 icra legged robots workshop presentation by robin deits." https://youtu.be/yagQG_b_hfs. Accessed: 2022-10-24.

[75] H. Dai and R. Tedrake, "Optimizing Robust Limit Cycles for Legged Locomotion on Unknown Terrain," in *Proceedings of the IEEE Conference on Decision and Control*, (Maui, Hawaii), p. 8, dec 2012.

[76] J. Zhu, N. J. Kong, G. Council, and A. M. Johnson, "Hybrid event shaping to stabilize periodic hybrid orbits," in *2022 International Conference on Robotics and Automation (ICRA)*, pp. 01–07, IEEE, 2022.

[77] P. E. Gill, W. Murray, and M. H. Wright, "Practical optimization (book)," *London and New York, Academic Press, 1981. 415 p*, 1981.

[78] Y. Hu, W. Wang, H. Jia, Y. Wang, Y. Chen, J. Hao, F. Wu, and C. Fan, "Learning to utilize shaping rewards: A new approach of reward shaping," *Advances in Neural Information Processing Systems*, vol. 33, pp. 15931–15941, 2020.

[79] G. Bledt, P. M. Wensing, and S. Kim, "Policy-regularized model predictive control to stabilize diverse quadrupedal gaits for the mit cheetah," in *2017 IEEE/RSJ International Conference on Intelligent Robots and Systems (IROS)*, pp. 4102–4109, IEEE, 2017.

[80] A. Hereid and A. D. Ames, "Frost: Fast robot optimization and simulation toolkit," in *2017 IEEE/RSJ International Conference on Intelligent Robots and Systems (IROS)*, pp. 719–726, IEEE, 2017.

[81] J. T. Betts, "Survey of numerical methods for trajectory optimization," *Journal of guidance, control, and dynamics*, vol. 21, no. 2, pp. 193–207, 1998.

[82] E. Philip, W. MURRAY, and M. A. SAUNDERS, "User's guide for snopt version 7: Software for large-scale nonlinear programming," 2015.